Journal of Nanobiotechnology

RESEARCH Open Access

New insights into allergic rhinitis treatment: MSC nanovesicles targeting dendritic cells

Jianyu Liu[1], Meiqun Wang[1], Xiaoyan Tian[1], Shuhong Wu[1], Haisen Peng[1], Yaqiong Zhu[1] and Yuehui Liu[1*]

Abstract

Allergic rhinitis (AR) is a condition with limited treatment options. This study investigates the potential use of mesenchymal stem cell (MSC) nanovesicles as a novel therapy for AR. Specifically, the study explores the underlying mechanisms of MSC nanovesicle therapy by targeting dendritic cells (DCs). The researchers fabricated DC-targeted P-D2-EVs nanovesicles and characterized their properties. Transcriptomic sequencing and single-cell sequencing analyses were performed to study the impact of P-D2-EVs on AR mice, identifying core genes involved in the treatment. In vitro cell experiments were conducted to validate the effects of P-D2-EVs on DC metabolism, Th2 differentiation, and ILC2 activation. The results showed that P-D2-EVs efficiently targeted DCs. Transcriptomic sequencing analysis revealed differential expression of 948 genes in nasal tissue DCs of mice treated with P-D2-EVs. Single-cell sequencing further revealed that P-D2-EVs had inhibitory effects on DC activation, Th2 differentiation, and ILC2 activation, with Fut1 identified as the core gene. Validation experiments demonstrated that P-D2-EVs improved IL10 metabolism in DCs by downregulating Fut1 expression, thereby suppressing Th2 differentiation and ILC2 activation. Animal experiments confirmed the inhibitory effects of P-D2-EVs and their ability to ameliorate AR symptoms in mice. The study suggests that P-D2-EVs reshape DC metabolism and suppress Th2 differentiation and ILC2 activation through the inhibition of the Fut1/ICAM1/P38 MAPK signaling pathway, providing a potential therapeutic approach for AR.

Keywords Allergic rhinitis, Mesenchymal stem cells, Dendritic cells, T helper 2 cells, Type 2 innate lymphoid cells, Single-cell sequencing

Introduction

Allergic rhinitis (AR) is a common immune-mediated disease characterized by inflammation and allergic reactions in the nasal mucosa, which significantly affects the quality of life and work efficiency of affected individuals [1–3]. Previous studies have shown that the occurrence and development of AR involve the activation and interaction of various immune cells [4, 5]. However, the existing therapeutic methods are not completely effective, thus highlighting the importance of identifying a new treatment strategy to improve the quality of life for patients [6–8].

Mesenchymal stem cells (MSCs), as a multifunctional cell type, hold great research value [9–11]. In recent years, it has been discovered that nanovesicles released by MSCs have therapeutic potential [12–14]. These nanovesicles contain a range of bioactive molecules that can regulate immune responses through interactions with other immune cells [15]. Therefore, nanovesicles could be a novel therapeutic strategy for the treatment of AR.

This study aimed to explore the possible mechanism of action of a novel MSCs nanovesicle, P-D2-EVs, in the treatment of AR by modulating the crosstalk between DCs, Th2, and ILC2 cells. By characterizing and analyzing P-D2-EVs in vitro and in vivo, we investigated the differential changes in DCs, Th2, and ILC2 in the nasal

*Correspondence:
Yuehui Liu
liuyuehuiclark@21cn.com
[1] Department of Otolaryngology Head and Neck Surgery, Jiangxi Medical College, Nanchang University, No. 1, Minde Road, Nanchang 330006, Jiangxi Province, China

tissues of AR mice before and after P-D2-EVs treatment. To study the potential of P-D2-EVs in AR therapy, we employed transcriptome sequencing and single-cell sequencing techniques [16–19]. Through bioinformatics analysis, we identified differentially expressed genes and verified their regulatory roles in AR development.

After P-D2-EVs treatment, we observed corresponding changes in the expression characteristics of DCs, Th2, and ILC2 in the nasal tissues of AR mice. Transcriptome sequencing and single-cell sequencing analyses revealed differential expression of key genes, including the important regulatory role of the Fut1 gene in AR treatment. Subsequent in vitro experiments validated the impact of P-D2-EVs on DC metabolism, Th2 differentiation, and ILC2 activation. Furthermore, in vivo animal experiments confirmed the therapeutic effects of P-D2-EVs, which reshaped DCs metabolism and inhibited Th2 differentiation and ILC2 activation by suppressing the Fut1/ICAM1/P38 MAPK signaling pathway, thus improving AR in mice.

This study not only contributes to a better understanding of the pathogenesis of AR but also provides novel strategies for its treatment by exploring the therapeutic potential of the new MSCs nanovesicle. Additionally, the application of nanovesicles as a drug delivery system holds significant clinical implications in enhancing drug targeting and efficacy. The results of this study can further refine the approach to AR treatment and contribute to improving the quality of life for patients.

Materials and methods

Extracellular vesicles (EVs) preparation from MSCs

Extracellular vesicles (EVs) were isolated from human umbilical cord MSCs (Procell, CP-CL11) using an ultracentrifugation method. Briefly, cells were cultured for three days in DMEM/F-12 medium (Gibco, 11320033) supplemented with fetal bovine serum (FBS, Vivacell, C3801-0100) to facilitate exosome secretion. The culture medium was collected and centrifuged at 300*g* and then 2000*g* for 15 min each at 4 °C to remove dead cells and cell debris. Subsequently, the supernatant was centrifuged at 20,000*g* for 30 min at 4 °C to remove insoluble impurities. The resulting solution was filtered through a 0.22 μm membrane filter (MerckMillipore, SLGP033RB). EVs were then extracted by centrifuging at 200,000*g* for 2 h at 4 °C. After washes with PBS (200,000*g*, 2 h), EVs were resuspended in a 5% trehalose PBS buffer (Beijing Bioassayon Biotechnology Co., Ltd., C1049) [20].

Preparation of modified P-D2-EVs

Modified P-D2 exosomes (P-D2-EVs) were prepared using a lipid hybrid technique. The P-D2 peptide (amino acid sequence: GGVTLTYQFAAGPRDK) was used for specific targeting of DCs. In brief, cholesterol (Solarbio, C8280), phospholipid (AVT, PC-98T), and DSPE-PEG-P-D2 synthesized by Hangzhou Xin Qiao Biotechnology Co., Ltd. were dissolved in 2 ml of tetrahydrofuran (Aladdin, 109-99-9) with an optimal weight ratio of 4:2:1. The mixture was then subjected to ultrasonication at 50 kHz for 30 min. Next, the solution was evaporated for 1 h on a rotary evaporator at 50 °C to remove the tetrahydrofuran. Subsequently, 1 ml of PBS was added, and the P-D2 liposomes were gently resuspended. Finally, the P-D2 liposomes were incubated with EVs at 37 °C for 15 min and subjected to multiple mild extrusions using a mini extruder (Avanti Polar Lipids, 610020) and a 200 nm pore size polycarbonate membrane (Avanti Polar Lipids, 610006) to form P-D2-EVs [20, 21]. As previously described, EVs were labeled with DiR covalently. EVs coupled with P-D2 peptide were purified using a Zeba spin desalting column (14K MWCO, ThermoFisher Scientific) equilibrated with PBS solution. The conjugation efficiency of P-D2 peptide on EVs was determined using 3-(4-carbpxubemzpul)quinoline-2-carboxaldehyde (CBQCA) (A6222, ThermoFisher Scientific) [22].

Characterization of EVs and P-D2-EVs

Transmission Electron Microscopy (TEM): 20 μL of EVs were dropped onto a copper grid and left to stand for 3 min. The liquid was then drawn from the side using filter paper. Afterward, 30 μl of pH 6.8 phosphotungstic acid solution (79690, Merck, USA) was added and allowed to rest for 5 min at room temperature. The sample was dried using an incandescent lamp and observed under a transmission electron microscope (JEM-1011, JEOL, Tokyo, Japan) with an accelerating voltage of 80 kV. Images were captured using the side-viewing Camera-Megaview III device (Soft Imaging System, Muenster, Germany).

Nanoparticle Tracking Analysis (NTA): EV samples were suspended in PBS and diluted 500-fold using Milli-Q water. Subsequently, the diluted EVs were injected into the sample chamber of a NanoSight LM10 (Malvern, UK) instrument using a sterile syringe, ensuring the absence of bubbles until the chamber was full. Video analysis was performed using NanoSight Version 2.3 (Malvern, UK) software with a gain of 6.0 and a threshold of 11. The movement trajectories of the particles were recorded, and dilution sample concentration and size distribution plots were generated. The EV concentration in the original solution was calculated based on the dilution factor.

Identification of EVs surface markers using Western blot: EVs were resuspended in radioimmunoprecipitation assay (RIPA) lysis buffer (Wuhan Asben Biological Technology Co., Ltd., China, AS1004), and surface markers CD9, CD81, CD63, and Alix, as well as endoplasmic

reticulum marker Calnexin, were detected through Western blot analysis. Antibody information can be found in the Western blot section below [23–26]. Each experiment was repeated three times.

Animals

Male SPF-grade BALB/c mice (6–8 weeks old) were obtained from Beijing Vitonlihua Experimental Animal Technology Co., Ltd (Beijing, China). The mice were housed in an SPF-grade animal laboratory with a humidity of 60–65% and a temperature of 22–25 °C and were subjected to a 12-h light–dark cycle. After one week of acclimation, the health condition of the mice was assessed prior to the start of the experiment [27].

Ethical statement

This study adhered strictly to ethical guidelines and regulations regarding animal experimentation. All experimental procedures were approved by the Institutional Animal Care and Use Committee (IACUC) with review number No. NCULAE-20221031024. The animals were housed and cared for in accordance with principles of humaneness, and experiments were performed with the utmost care to minimize pain and distress. At the end of the experiment, all mice were euthanized in a humane manner under ethyl ether anesthesia.

Establishment and grouping of a mouse model for AR

One hundred BALB/c mice were obtained and randomly assigned to two groups: the Control group (18 mice) and the Model group (81 mice). The Model group was induced with ovalbumin (OVA) to develop an AR mouse model. Briefly, BALB/c mice were sensitized with 200 μl of PBS (containing 50 μg OVA from Sigma-Aldrich, 01641, and 2 mg aluminum hydroxide from Solarbio, IA5810) via intraperitoneal injection on days 0, 7, and 14. From day 21 to day 27, mice were intranasally challenged with 20 μl of PBS (containing 400 μg OVA) to induce allergic reactions. The number of nose itching (rubbing) and sneezing events within 2 h after the last intranasal OVA administration were recorded and evaluated. Specifically, we calculated the number of sneezing episodes, duration of rhinorrhea, and frequency of nose scratching or rubbing in mice of the experimental and control groups within 2 h after the last intranasal OVA administration. Statistical analysis using a t-test was conducted to assess the significant differences in the occurrence of these symptoms between the control and experimental groups [28, 29], aiming to confirm the successful establishment of the AR mouse model. Mice in the Control group only received intraperitoneal injection and intranasal PBS administration [30–32].

Subsequently, the Model group was randomly divided into the following 10 groups: Model + PBS group (3 mice), Model + DiR-EVs group (3 mice), Model + DiR-P-D2-EVs group (3 mice), Model group (6 mice), Model + EVs group (6 mice), Model + P-D2-EVs group (6 mice), Model + NC-OE-mDCs group (6 mice), Model + Fut1-OE-mDCs group (6 mice), Model + P-D2-EVs + NC-OE-mDCs group (6 mice), and Model + P-D2-EVs + Fut1-OE-mDCs group (6 mice).

In the Model + PBS group, on the 28th day after the successful establishment of the AR model, intranasal administration of 20 μl PBS was conducted. In the Model + DiR-EVs group, on the 28th day, intranasal administration of 20 μl PBS (containing 250 μg DiR-labeled EVs) was performed. The DiR labeling was carried out using the DiR fluorescent dye (Noninbio, NW3201) according to the manufacturer's instructions prior to administration. In the Model + DiR-P-D2-EVs group, intranasal administration of 20 μl PBS (containing 250 μg DiR-labeled P-D2-EVs) was conducted on the 28th day. In vivo, fluorescence imaging was performed using an in vivo imaging system (IVIS) at fixed time points [20, 27].

In addition, the Model group received no further treatment after the AR model establishment and was euthanized on day 28 after anesthesia with pentobarbital sodium (80 mg/kg, Sigma-Aldrich, P3761). For the Model + EVs group, apart from intranasal administration of 20 μl PBS (containing 400 μg OVA and 250 μg EVs) from days 21 to 27, the procedures were the same as those for the Model group. The Model + P-D2-EVs group intranasally received 20 μl PBS (containing 400 μg OVA and 250 μg P-D2-EVs) from days 21 to 27 [27].

In addition, in the Model + NC-OE-mDCs group, on the 16th and 18th days of establishing the AR model, 1×10^6 bone marrow-derived mature DCs, transfected with adeno-associated virus empty vector (NC-OE), were transferred to the nasal cavity of mice. The procedures were the same as in the Model group. In the Model + Fut1-OE-mDCs group, on the 16th and 18th days, 1×10^6 mature DCs transfected with adeno-associated virus vector overexpressing Fut1 (Fut1-OE) were transferred to the nasal cavity of mice. The procedures were the same as in the Model group. In the Model + P-D2-EVs + NC-OE-mDCs group, on the 16th and 18th days, 1×10^6 NC-OE-mDCs were transferred to the nasal cavity of mice. The procedures were the same as in the Model + P-D2-EVs group. In the Model + P-D2-EVs + Fut1-OE group, on the 16th and 18th days, 1×10^6 Fut1-OE-mDCs were transferred to the nasal cavity of mice. The procedures were the same as in the Model + P-D2-EVs group. Detailed methods for preparing NC-OE or Fut1-OE transfected mDCs are described

in the following section on cell culture and cell grouping [33].

Moreover, the remaining 10 untreated BALB/c mice were used to extract bone marrow DCs and primary $CD4^+$ T cells from the spleen. Three mice from the Model + PBS group, Model + DiR-EVs group, and Model + DiR-P-D2-EVs group were used for in vivo fluorescence imaging. Three mice, each from the Model group and Model + P-D2-EVs group, were used for single-cell sequencing, while an additional three mice were used for transcriptome sequencing. Each group, including the Control group, Model group, Model + EVs group, Model + P-D2-EVs group, Model + NC-OE-mDCs group, Model + Fut1-OE-mDCs group, Model + P-D2-EVs + NC-OE-mDCs group, and Model + P-D2-EVs + Fut1-OE-mDCs group, consisted of six mice for detecting AR-related indicators, except for the Model + EVs group, an additional three mice were used in each group for flow cytometry to detect the proportion of target cells and relevant gene expression [30–32].

In vivo fluorescence imaging

Following the establishment of the AR model, animal grouping was conducted on Day 28 as follows: Model + PBS group, Model + DiR-EVs group, and Model + DiR-P-D2-EVs group. According to the description of the animal groups, these groups received intranasal administration of PBS EVs labeled with DiR and P-D2-EVs, respectively. In vivo, fluorescence imaging of the mice was performed at 6 and 12 h after drug administration using the IVIS Lumina III in vivo imaging system (PerkinElmer, CLS136334). Prior to imaging, the mice underwent brief anesthesia to ensure their immobility during the procedure [20, 34].

Detection of in vivo DC uptake of P-D2-EVs using flow cytometry

We analyzed the distribution of P-D2-EVs within DCs in nasal tissues of AR mice using in vivo fluorescence imaging. We utilized antibodies labeled with FITC against surface markers of anti-Mouse CD11c (BD, 568942), MHC-II (CST, 42594S), CD80 (BD, 553768), and CD86 (BD, 561962) to perform DC sorting on the Cytek Aurora Flow Cytometer (Cytek). Subsequently, we determined the cellular percentages of DiR-labeled EVs and P-D2-EVs uptake [20, 35, 36].

Flow cytometric analysis

First, single cells were prepared by enzymatic digestion of nasal tissue. The cell suspension was lysed using an ACK lysis buffer (ThermoFisher, A1049201), and dead cells that stain positive for 7-AAD reagent (CST, 72782S) were excluded. Antibodies against surface markers of DCs, including FITC-labeled anti-Mouse CD11c, MHC-II, CD80, and CD86, as well as Alexa Fluor™ 488-labeled anti-Mouse Ki67 (ThermoFisher, 53-5698-82), PE-labeled anti-Mouse IL10 (ThermoFisher, 12-7101-82), Alexa Fluor™ 532-labeled anti-Mouse CD3 (ThermoFisher, 58-0032-82), APC-eFluor™ 780-labeled anti-Mouse CD4 (ThermoFisher, 47-0042-82), APC-labeled anti-Mouse IL4 (ThermoFisher, 17-7041-82), Alexa Fluor™ 700-labeled anti-Mouse GATA3 (ThermoFisher, 56-9966-42), PerCP-Cy™5.5-labeled Mouse Lineage Antibody Cocktail (BD, 561317), BV711-labeled Anti-Mouse CD90.2 (BD, 740647), PE-Cy™ 7-labeled anti-Mouse CD45 (BD, 552848), BUV563-labeled anti-Mouse KLRG1 (BD, 741343), and eFluor™ 660-labeled anti-Mouse IL13 (ThermoFisher, 50–7133-82) were incubated with the cells. CD11c, MHC-II, CD80, and CD86 were surface markers for DCs, Ki67 was an activation marker for DCs, IL10 was a cytokine for DCs, CD3 + CD4 + IL4 + represented Th2 cells, GATA3 was a marker for Th2 cell differentiation and ILC2 activation, and Lineage-CD45 + KLRG1 + CD90.2 + represented ILC2 cells, while IL13 was a cytokine for ILC2 cells. After adding the antibodies, cells were incubated at 4 °C in the dark for 30 min. The cells were then washed twice with PBS and centrifuged at 2000 g for 5 min at 4 °C. Percentages of labeled markers were analyzed using the Cytek Aurora Flow cytometer (Cytek) [20, 35–39].

In vitro extracellular vesicle uptake

To label EVs and P-D2-EVs, the PKH67 green fluorescent cell linker mini kit (Sigma-Aldrich, MINI67-1KT) was employed as per the kit's instructions. Next, the DCs isolated from nasal tissue through flow cytometry were seeded in a 24-well plate at a concentration of 4×10^4 cells per well. The plate was incubated overnight at 37 °C with 5% CO_2 following thorough mixing. The supernatant was then discarded, and DMEM/F-12 medium containing exosome-free FBS was added to each well. Approximately 10 μg of PKH67-labeled EVs or P-D2-EVs was added to each well and thoroughly mixed. The plate was placed in a cell culture incubator for a total of 2 or 8 h. After the incubation period, the cells were collected and seeded on poly-L-lysine-treated slides for 30 min for adherence. CellMembrane staining was performed using CellMask™ Cell Membrane Stain (Invitrogen, C10046) following the manufacturer's instructions to label the cell membrane of DCs after uptake of EVs or P-D2-EVs. The cells were then treated with PBS containing 0.1% Triton X-100 (Sigma-Aldrich, X100) for 5 min, followed by three washes with PBS. Finally, the slides were mounted using a mounting medium containing DAPI (Beyotime, P0131-5 ml) and observed and photographed under a Zeiss LSM 880 confocal fluorescence microscope (Carl

Zeiss). The fluorescence intensity of three independent fields of view was quantified using ImageJ software for each group [35, 40].

Cellular analysis of NALF and serum immunoglobulin E (IgE)

NALF and serum were collected from euthanized mice prior to anesthesia. After anesthetizing the mice, the upper position of the trachea was ligated, and then 1 ml of cold PBS was gently injected into the nasopharynx using a size 21 cannula. The collected NALF was centrifuged at 3000 g for 5 min at 4 °C. The cellular pellet of NALF was resuspended in PBS, and 50 μl of the cell suspension was smeared onto glass slides, followed by staining using the Diff-Quick staining kit (Solarbio, G1540). The total cell count was determined using ImageJ software, with 3 independent fields counted for each group. Blood was collected from the inferior vena cava, allowed to clot for 2–3 h at room temperature, and then centrifuged at 3000*g* for 5 min at 4 °C to obtain serum. OVA-specific IgE levels in the serum were measured using the ELISA kit (Bioswamp, MU30065) [36].

Nasal tissue pathology

After the nasal tissues from the mice were collected, they were fixed in 10% neutral formalin (Biosharp, BL388A) for 48 h and embedded in paraffin. Subsequently, 4 μm thick paraffin sections were prepared (three sections per mouse), and hematoxylin and eosin (H&E) staining was performed using the staining kit (Solarbio, G1120) to evaluate the infiltration of nasal eosinophils. Immunohistochemical staining was also carried out using the anti-Mouse NIMP-R14 antibody (Abcam, ab2557) as a neutrophil marker, followed by incubation with Goat anti-Rat-HRP secondary antibody (ThermoFisher, 31470) and substrate 3,3′-diaminobenzidine (Sigma-Aldrich, D8001), resulting in brown staining of positive cells. A periodic acid-Schiff (PAS) staining kit (Beyotime, C0142S) was utilized to determine the percentage of PAS-positive goblet cells. Images were observed under an inverted microscope (Olympus, BX63), and ImageJ software was used to quantify the nasal mucosal thickness, eosinophil and neutrophil counts, and the percentage of goblet cells [32, 36, 41]. Three independent fields were quantified for each section.

RNA extraction, library construction, and sequencing

Total RNA was extracted from dendritic cells (DCs) isolated from nasal tissues of mice in the Model group (n = 3) and the Model + P-D2-EVs group (n = 3) using Trizol reagent (15596026, Invitrogen, USA) through flow cytometry. The concentration and purity of RNA samples were measured using the Nanodrop 2000 spectrophotometer (1011U, nanodrop, USA). Total RNA samples meeting the following criteria were used for subsequent experiments: RNA integrity number (RIN) ≥ 7.0 and 28S:18S ratio ≥ 1.5 [35, 42].

Sequencing libraries were generated and sequenced by CapitalBio Technology (Beijing, China). A total of 5 μg RNA was used for each sample. In brief, the Ribo-Zero magnetic kit (MRZE706, Epicentre Technologies) was used to remove ribosomal RNA (rRNA) from total RNA. NEB Next Ultra RNA library preparation kit (#E7775, NEB, USA) was used to construct libraries for Illumina sequencing. Then, the RNA was fragmented into approximately 300 base pair (bp) fragments using NEB Next first strand synthesis reaction buffer (5×). First-strand cDNA was synthesized using reverse transcriptase primers and random primers, followed by second-strand cDNA synthesis using second-strand synthesis reaction buffer in the presence of dUTP Mix (10×). The cDNA fragments were end-repaired, including the addition of polyA tails and the connection of sequencing adapters. After adapter ligation, the USER enzyme (#M5508, NEB, USA) was used to digest the second strand of cDNA to construct strand-specific libraries. Library DNA was amplified, purified, and enriched using PCR. Finally, the libraries were assessed using Agilent 2100 and quantified using the KAPA library quantification kit (KK4844, KAPA Biosystems). Pair-end sequencing was performed on the NextSeqCN500 (Illumina) sequencer [35, 42].

Quality control of sequencing data and alignment to the reference genome

The quality of paired-end reads in the raw sequencing data was examined using FastQC software v0.11.8. The original data was preprocessed using Cutadapt software 1.18 to remove Illumina sequencing adapters and poly(A) tail sequences. Perl scripts were utilized to eliminate reads with an N content exceeding 5%. The FASTX Toolkit software 0.0.13 was employed to extract reads with a base quality of 20 or above, accounting for 70% of the bases. BBMap software was used to repair the paired-end sequences. Lastly, the filtered high-quality read fragments were aligned against the mouse reference genome using Hisat2 software version 0.7.12 [43, 44].

Sample preparation and sequencing of single cells

Three Model mice and three model + P-D2-EVs mice were selected, and nasal tissue samples were collected. The nasal tissue samples were prepared as single-cell suspensions and loaded onto Chromium Single Cell chips. The Chromium Single Cell 3′ v3 kit (10 × Genomics) was used to prepare the samples according to the manufacturer's instructions, capturing approximately 10,000 individual cells per sample. During cDNA synthesis, the

captured mRNA was barcode labeled. Subsequently, the single-cell RNA-seq libraries for Illumina sequencing were prepared using the Chromium Single Cell 3′ Solution (10×Genomics) following the manufacturer's instructions. Barcode labeling was performed using Illumina Sample Indexes, and sequencing was conducted on a single Illumina flow cell channel using the Illumina HiSeq 4000 sequencer. The sequencing parameters were as follows: Read 1 contained 28 bases, Read 2 contained 98 bases, and the sample index included 8 bases. The minimum number of reads per cell sequenced from the RNA library was set at 25,000 [45].

TSNE clustering analysis, cell annotation, pseudotime analysis, and cell communication analysis

In this study, scRNA-seq data was analyzed using the "Seurat" package in R software. A series of quality control measures were initially performed, including the following filtering conditions: nFeature_RNA > 200, nFeature_RNA < 5000 percent.mt < 10. Batch effects were eliminated using the canonical correlation analysis (CCA) method, followed by standardization of the data using the LogNormalize function.

To reduce the dimensionality of the scRNA-seq dataset, principal component analysis (PCA) was applied to the highly variable genes based on the top 2000 genes with the highest variance. The first 30 principal components were then selected for TSNE clustering analysis. The FindClusters function provided by Seurat was employed to identify the main cell subgroups, with a default resolution value of res = 0.9. Subsequently, the UMAP algorithm was used to reduce nonlinear dimensionality of the scRNA-seq sequencing data. Cell type-specific marker genes were identified for various cell subgroups using the Seurat package. Furthermore, the "SingleR" package was utilized to annotate the marker genes of each cell cluster, with reference data sets loaded using the MouseRNAseqData function. Cell annotation was carried out by considering known cell lineage-specific marker genes and utilizing the CellMarker online website.

Subsequently, the "monocle" package in R software was employed for pseudotime analysis. Cell communication analysis was performed using the "cellchat" package [46].

Bioinformatics analysis of differentially expressed genes in transcriptome and single-cell sequencing

Differential expression gene (DEG) identification was performed on the raw count matrix of DCs transcriptome sequencing using the "limma" package in the R language. A threshold of |log fold change (FC)| > 2 and P-value < 0.05 was chosen, and a volcano plot was generated using the "ggplot2" package. A heatmap of the DEGs was created using the "pheatmap" package. Subsequently, the R packages "clusterProfiler", "org.Hs.eg.db", "org.Mm.eg.db", "enrichplot", "ggplot2", and "pathview" were utilized for Gene Ontology (GO) and Kyoto Encyclopedia of Genes and Genomes (KEGG) analyses [47].

The DCs cell subpopulation was extracted from the single-cell data, and the "limma" package in the R language was employed to identify differentially expressed genes (ScRNA-DEGs) with a threshold of |log fold change (FC)| > 0.5 and P-value < 0.05. The "EnhancedVolcano" package was used to generate a volcano plot. A Venn diagram was created using the Jvenn website to obtain the differentially expressed genes (B-DEGs) that intersected with DEGs and ScRNA-DEGs. KEGG and GO analyses were then performed [48].

RT-qPCR

RNA was extracted from ruptured cells or nasal tissue using the Trizol reagent kit (Invitrogen, 10296028CN). The quality and concentration of RNA were determined by UV–visible spectrophotometry using the ND-1000 NanoDrop (USA). To measure mRNA expression, reverse transcription was carried out using the PrimeScript™ RT-qPCR kit (TaKaRa, RR037Q). Real-time quantitative reverse transcription polymerase chain reaction (RT-qPCR) was performed on a LightCycler 480 system (Roche Diagnostics, Pleasanton, CA, USA) using SYBR Premix Ex Taq™ (TaKaRa, RR390A). The reference gene GAPDH was used as an internal control for mRNA expression. Primer design and synthesis were provided by Shanghai Universal Biotech Co., Ltd. Primer sequences can be found in Table S1. The relative expression of the target gene in the experimental group compared to the control group was determined using the $2^{-\Delta\Delta Ct}$ method, where ΔΔCT = ΔCt experimental group − ΔCt control group, and ΔCt = target gene Ct − reference gene Ct [35].

Cell culture

To isolate DCs from the bone marrow of BALB/c mice, the mice were euthanized by cervical dislocation, and then soaked in a 75% ethanol solution for 5 min. The femur and tibia were extracted, and the bone marrow cavity was rinsed with sterile PBS three times to obtain a cell suspension. The suspension was filtered through a 200-mesh cell strainer (Corning, 352,350) to remove small bone fragments and muscle tissues, followed by centrifugation at 1200*g* for 5 min. The supernatant was removed, and the remaining cells were treated with red blood cell lysis buffer (Solarbio, R1010) for 3 min, followed by centrifugation to collect the bone marrow cells (BM cells). After counting the BM cells, they were seeded in a 24-well plate at a concentration of 1×10^6/ml in RPMI 1640 medium (Gibco, 11875093) containing 10% fetal bovine serum (FBS, Gibco, USA) and 1% penicillin/

streptomycin, supplemented with 20 ng/ml GM-CSF (MCE, HY-P7361) and 20 ng/ml IL-4 (MCE, HY-P70644) dissolved in PBS. The cells were incubated at 37 °C with 5% CO_2. On the 3rd and 5th days, half of the medium was replaced with a fresh medium containing the same concentration of cytokines. After 5 days of culture, cells were harvested, and the phenotype of immature DCs (iDCs) was analyzed by flow cytometry. Additionally, on the 5th day, 100 ng/ml of LPS (MCE, HY-D1056) dissolved in PBS was added to the culture medium for 2 days to collect non-adherent cells, referred to as mature DCs (mDCs). The collected cells were suspended in ice-cold flow cytometry buffer (ThermoFisher, 00-4222-26) and characterized as immature and mature DCs using flow cytometry with antibodies targeting DC surface markers CD11c, MHC-II, CD80, and CD86 [35, 41, 49].

The spleens were removed to isolate $CD4^+$ T cells from the spleens of BALB/c mice. The Mouse Spleen Dissociation Kit (Miltenyi Biotec, 130-095-926) was used according to the manufacturer's instructions to prepare single-cell suspensions from the spleen. The Mouse Naïve $CD4^+$ T cell Isolation Kit (Miltenyi Biotec, 8804-6824-74) was used according to the manufacturer's instructions to isolate naïve $CD4^+$ T cells from mouse splenocytes. Mouse $CD4^+$ T cells (3×10^5 cells/ml) were co-cultured with DCs treated in different ways for 5 days. The medium used was RPMI 1640 supplemented with 10% FBS, 1% penicillin/streptomycin, and IL-2 (100 IU/ml, Beyotime, P5907) [38, 50].

ILC2 cells were sorted from the nasal-associated lymphoid tissue (NALT) of OVA-sensitized mice. On day 28, OVA-sensitized mice were euthanized, and the NALT was transferred to RPMI 1640 medium for further processing. The cells were passed through a 40 μm cell strainer (Fisher Scientific, FIS22-363-547). Red blood cells were lysed using red blood cell lysis buffer at room temperature for 2–5 min. Subsequently, the cells were washed with 10 ml of PBS, centrifuged for 5 min, and resuspended in 10 ml of RPMI 1640 medium. ILC2 cells were isolated using the EasySep™ Mouse ILC2 Enrichment Kit (Miltenyi Biotec, 19842) according to the manufacturer's instructions. The sorted cells were then cultured at 37 °C for 6 days in a medium containing 10% FBS, 0.1% β-mercaptoethanol (ThermoFisher, 31350010), 1% penicillin/streptomycin, and 10 ng/ml of mouse recombinant IL-33 (Abcam, ab187455), IL-7 (Abcam, ab270065), and TSLP (Abcam, ab310786) [39].

Cell grouping

Firstly, cells extracted from BALB/c mouse bone marrow were induced into three different types of iDCs using different treatments: the BM cells group, the iDCs group, and the iDCs + P-D2-EVs group. In the BM cells group, bone marrow cells were co-cultured with PBS for 5 days. In the iDCs group, bone marrow cells were co-cultured with GM-CSF, IL-4, and PBS for 5 days. In the iDCs + P-D2-EVs group, bone marrow cells were co-cultured with GM-CSF, IL-4, and 3×10^9/ml P-D2-EVs for 5 days [35, 51].

Next, BALB/c mouse bone marrow cells were treated or induced using different methods, resulting in twelve different types of mDCs: the iDCs group, the mDCs group, the mDCs + P-D2-EVs group, NC-OE-iDCs, Fut1-OE-iDCs, NC-OE-mDCs, Fut1-OE-mDCs group, NC-OE-mDCs + P-D2-EVs group, Fut1-OE-mDCs + P-D2-EVs group, Fut1-OE-mDCs + 2DGal group, mDCs + 2DGal group, and mDCs + 2DGal + Anisomycin group.

In the iDCs group, bone marrow cells were co-cultured with GM-CSF and IL-4 from day 1 to 7, followed by PBS treatment from day 5 to 7. Both the mDCs group and mDCs + P-D2-EVs group conducted cell counting on day 5, adjusting the concentration of P-D2-EVs based on the ratio of 1000 EVs internalized per cell. The cell density of various mDC types on day 5 was approximately $2–3\times10^5$/ml. From day 5 to 7, LPS and PBS or LPS, along with P-D2-EVs based on the 1000 EVs per cell standard, were added. Subsequent cell experiments involving P-D2-EVs were treated in accordance with this standard. In the mDCs + 2DGal group, 2-deoxy-D-galactose (10 mM; MCE, HY-131892) was additionally induced from day 5 to 7. In the mDCs + 2DGal + Anisomycin group, both 2DGal and Anisomycin (0.5 μM; MCE, HY-18982) were induced from day 5 to 7 [52, 53].

Furthermore, plasmids overexpressing the mouse Fut1 gene (Ad-Fut1, Fut1-OE) and plasmids for knocking down the mouse Fut1 gene were synthesized by HanBio. Fut1-OE and adenoviral empty vector (NC-OE), as well as sh-Fut1 and sh-NC, were separately transfected into human embryonic kidney cell line AD293 (Agilent, 240085) for viral packaging using LipoFiter transfection reagent (HanBio, HB-LF-1000). Supernatant containing viruses was collected 72 h later. High titer adenovirus was purified using Vivapur® AdenoPACK™ 20 kit (Sartorius, VS-AVPQ022) and subsequently titrated by endpoint dilution method. Following 5 days of incubation with GM-CSF and IL-4, iDCs were seeded into 24-well plates at a concentration of 10^6 cells per well. The cells were then infected with Fut1-OE or NC-OE, as well as sh-Fut1 and sh-NC at multiplicities of infection (MOI) of 10, 50, 100, or 1000. After 4 h of transfection, the transfection medium was replaced with fresh culture medium and incubated for an additional 18 h. Subsequently, LPS was used to induce iDCs into mDCs [54, 55].

NC-OE-iDCs/sh-NC-iDCs were transfected for 4 h before being switched to a fresh culture medium for an 18-h incubation. Likewise, Fut1-OE-iDCs/sh-Fut1-iDCs

underwent transfection and subsequent culture change. The NC-OE-mDCs/sh-NC-mDCs group was subjected to continued induction with LPS and PBS for 2 days following the transfection of NC-OE-iDCs/sh-NC-mDCs. Similarly, the Fut1-OE-mDCs/sh-Fut1-mDCs group received the same induction with LPS and PBS post-transfection of Fut1-OE-iDCs/sh-Fut1-iDCs. The group NC-OE-mDCs + P-D2-EVs was maintained with LPS + P-D2-EVs induction after the NC-OE-iDCs/sh-NC-iDCs transfection. Moreover, the group Fut1-OE-mDCs + P-D2-EVs/sh-Fut1-mDCs + P-D2-EVs underwent the same induction with LPS + P-D2-EVs post-transfection of Fut1-OE-iDCs/sh-Fut1-iDCs. Finally, the group Fut1-OE-mDCs + 2DGal was induced with LPS and 2DGal following the transfection of Fut1-OE-iDCs [52, 54, 55].

In the $CD4^+$ T group, only $CD4^+$ T cells were cultured for 5 days without the addition of mDCs, with an equal amount of culture medium. In the $CD4^+$ T + mDCs group, mDCs were co-cultured with $CD4^+$ T cells in a ratio of 1:10 for 5 days. The $CD4^+$ T + P-D2-EV-mDCs group indicates the co-culturing of P-D2-EV-mDCs with $CD4^+$ T cells. The $CD4^+$ T + NC-OE-mDCs group signifies the co-culturing of NC-OE-mDCs with $CD4^+$ T cells. The $CD4^+$ T + P-D2-EV-NC-OE-mDCs group involves the co-culturing of P-D2-EV-NC-OE-mDCs with $CD4^+$ T cells. The $CD4^+$ T + Fut1-OE-mDCs group demonstrates the co-culturing of Fut1-OE-mDCs with $CD4^+$ T cells. The $CD4^+$ T + P-D2-EV-Fut1-OE-mDCs group denotes the co-culturing of P-D2-EV-Fut1-OE-mDCs with $CD4^+$ T cells [38, 50].

Additionally, in the $CD4^+$ T + anti-IL10Rα + P-D2-EV-mDCs group, $CD4^+$ T cells were pre-treated with IL10Rα blocking antibody (5 μg/ml, R&D, AF-474-NA) for 30 min before co-culturing. In the $CD4^+$ T + anti-IL10 + P-D2-EV-mDCs group, an additional anti-mouse IL10 monoclonal antibody was added during co-culturing (75 ng/ml, R&D, MAB417-SP). The $CD4^+$ T + IL10 + Fut1-OE-mDCs group involved the additional addition of IL10 (10 ng/ml, Solarbio, P00104) during co-culturing [35, 38].

Finally, the supernatant of the co-cultured mDCs and $CD4^+$ T cells was divided into 8 groups for co-culture with ILC2, namely ILC2 + $CD4^+$ T, ILC2 + $CD4^+$ T + mDCs, ILC2 + $CD4^+$ T + P-D2-EV-mDCs, ILC2 + IL4 + $CD4^+$ T + P-D2-EV-mDCs, ILC2 + $CD4^+$ T + NC-OE-mDCs, ILC2 + $CD4^+$ T + Fut1-OE-mDCs, ILC2 + anti-IL4 + $CD4^+$ T + Fut1-OE-mDCs, and ILC2 + anti-IL4Rα + $CD4^+$ T + Fut1-OE-mDCs.

In the ILC2 + $CD4^+$ T group, the supernatant from the $CD4^+$ T group was co-cultured with ILC2 for 3 days. In the ILC2 + $CD4^+$ T + mDCs group, the supernatant from the $CD4^+$ T + mDCs group was co-cultured with ILC2. In the ILC2 + $CD4^+$ T + P-D2-EV-mDCs group, the supernatant from the $CD4^+$ T + P-D2-EV-mDCs group was co-cultured with ILC2. In the ILC2 + IL4 + $CD4^+$ T + P-D2-EV-mDCs group, an additional 20 ng/ml IL-4 was added during co-culturing. In the ILC2 + $CD4^+$ T + NC-OE-mDCs group, the supernatant from the $CD4^+$ T + NC-OE-mDCs group was co-cultured with ILC2. In the ILC2 + $CD4^+$ T + Fut1-OE-mDCs group, the supernatant from the $CD4^+$ T + Fut1-OE-mDCs group was co-cultured with ILC2. In the ILC2 + anti-IL4 + $CD4^+$ T + Fut1-OE-mDCs group, an additional 100 ng/ml IL-4 and anti-IL4 antibody (ThermoFisher, MA5-23,722) were added during co-culturing. In the ILC2 + anti-IL4Rα + $CD4^+$ T + Fut1-OE-mDCs group, an IL-4Rα blocking antibody (1 μg/ml, Santa Cruz Biotechnology, sc-28361) was added during co-culturing [35, 38, 56].

Intracellular cytokine staining of extracellular cells using flow cytometry

For intracellular cytokine staining, cells were first fixed with 4% paraformaldehyde (Biosharp, BL539A) for 20 min, followed by permeabilization using eBioscience™ Intracellular Fixation & Permeabilization Buffer (ThermoFisher, 88-8824-00). The fixed and permeabilized cells were then resuspended in eBioscience™ Flow Cytometry Staining Buffer (ThermoFisher, 00-4222-57) and co-incubated with the following antibody markers in the dark for 30 min: PE-conjugated IL10 (ThermoFisher, 12-7101-82), APC-conjugated IL4 (ThermoFisher, 17-7041-82), Alexa Fluor™ 700-conjugated GATA3, eFluor™ 660-conjugated IL13 (ThermoFisher, 50-7133-82), and eFluor™ 450-conjugated IL5 (ThermoFisher, 48-7052-82). After co-incubation, cells were washed twice with FACS washing buffer and subjected to differential expression analysis using an LSRII Fortessa flow cytometer (BD Biosciences). Data obtained were analyzed using FlowJo-X software [57].

ELISA

Mouse serum or cell culture supernatant was collected and the levels of IL-10, IL-4, IL-13, and IL-5 were quantified using Mouse ELISA kits purchased from ThermoFisher (IL-10: BMS614, IL-4: BMS613, IL-13: BMS6015, IL-5: M551). The assays were performed according to the manufacturer's instructions to measure the concentrations of IL-10, IL-4, and IL-13 in the serum or cell culture supernatant [35].

Western blot

RIPA total protein lysis buffer (AS1004, Wuhan Aspen Biotechnology Co., Ltd.) was used to lyse EVs, P-D2-EVs, and cells. The protein concentrations were measured using the BCA protein quantitation assay kit (Thermo

Fisher, 23227). The proteins were separated by SDS-PAGE and transferred to a PVDF membrane, which was blocked with 5% BSA at room temperature for 1 h. Subsequently, the following primary antibodies, diluted as indicated, were added: CD9 (1:1000, Abcam, ab307085), CD81 (1:1000, Abcam, ab109201), CD63 (1:1000, Abcam, ab134045), Alix (1:1000, Abcam, ab275377), Calnexin (1:20,000, Abcam, ab92573), Fut1 (1:500, Proteintech, 17956-1-AP), ICAM1 (1:250, Thermo Fisher, MA5407), UEA1 antibody (1:500, BIOSS, bs-10025R), p-P38 MAPK (1:1000, CST, #9212), P38 MAPK (1:1000, CST, #9211), and GAPDH (1:10,000, Thermo Fisher, AM4300). The primary antibodies were incubated overnight at 4 °C.

CD9, CD81, CD63, and Alix are markers of EVs, while Calnexin is a marker of the endoplasmic reticulum membrane. FUT1 and ICAM1 serve as key regulatory proteins, and UEA1 specifically recognizes α-(1,2)-fucose glycans. p-P38 MAPK and P38 MAPK are markers of the P38 MAPK signaling pathway.

The membrane was washed three times with TBST (5 min each wash) and then incubated at room temperature for 2 h with the appropriate secondary antibodies: Anti-Mouse-HRP (1:10,000, Thermo Fisher, 31430) or Goat anti-Rabbit-HRP (1:10,000, Thermo Fisher, 31460). Afterwards, the membrane was washed three times with TBST (5 min each wash). TBST was removed, and an appropriate amount of ECL working solution (Millipore, WBKLS0500) was added, followed by incubation at room temperature for 1 min. Excess ECL reagent was removed, and the membrane was sealed with plastic wrap, placed in a dark box, and exposed to X-ray film for 5–10 min. The film was then developed and fixed. Image J software was used for densitometric analysis of the Western blot bands, with GAPDH used as an internal reference [38].

Enrichment experiment of *Ulex* europaeus agglutinin 1 (UEA1)

To collect different treated cell lines, we lysed the cells using NP40 cell lysis buffer (ThermoFisher, FNN0021) supplemented with a protease inhibitor (ThermoFisher, A32953). The cell lysate (1000 μg) was then mixed with 100 μl of UEA1 (0.1 μg/ml; Xian QiYue Biotechnology Co., Ltd., Q-0003008) labeled with biotin. The mixture was incubated overnight at 4℃ with gentle rotation. Streptavidin Agarose (ThermoFisher, SA10004) beads were added, containing an affinity for biotin, and the incubation was continued for another 4 h. The samples were extracted and separated by SDS-PAGE and then transferred onto a PVDF membrane. The membrane was incubated with antibodies against FUT1, ICAM1, and GAPDH, with GAPDH serving as a control. The antibody information is consistent with the Western blot section. FUT1 and ICAM1 were used to detect the total protein in different input samples, while ICAM1 was also used to assess the level of ICAM1 fucosylation after UEA1 enrichment [52, 58].

Immunoprecipitation (IP)

Immunoprecipitation was performed according to the manufacturer's instructions using the Protein A Immunoprecipitation Kit (Beyotime, 2006). mDCs cells subjected to different treatments were lysed using NP40 cell lysis buffer supplemented with protease inhibitors and incubated on ice for 1 h. The lysates containing proteins were incubated overnight at 4 °C with Sepharose beads coupled with primary antibodies against ICAM1 and UEA1. The proteins were eluted by the lysing buffer, resuspended in SDS sample buffer, and subsequently analyzed by Western blot. The antibody information was consistent with the Western blot results [58].

Immunofluorescence staining

Cells were cultured on glass slides and fixed with 4% paraformaldehyde. Cell membranes were permeabilized with 0.5% Triton X-100 (Sigma-Aldrich, X100), and non-specific binding was blocked with BSA (Solarbio, SW3015). Slides were incubated overnight with primary antibodies against ICAM1 (Thermofisher, MA5-43106) at a dilution of 1:60. After washing with PBST, cells were incubated with Alexa Fluor™ 594 goat anti-rabbit IgG secondary antibody (Thermofisher, A-11012) at a concentration of 2 μg/ml. Following a PBST wash, FITC-labeled UEA1 (Thermofisher, L32476) was used for UEA1 staining at a concentration of 5 μg/ml for 1 h at 37 °C. Nuclei were counterstained with DAPI (Invitrogen, D3571) for 5 min at room temperature, and then the slides were sealed. ICAM1 and UEA1 co-localization fluorescence intensities were quantitatively analyzed using ImageJ software with three independent fields of view for each group under an Olympus BX40 fluorescence microscope [59, 60].

Statistical analysis

All experiments were conducted independently at least three times, and the data are presented as the mean ± SD (standard deviation). Independent samples t-test or one-way analysis of variance (ANOVA) were employed to compare differences between groups. If the ANOVA results indicated significant differences, further Tukey's honestly significant difference (HSD) post-hoc tests were conducted to compare differences among individual groups. For non-normal distribution or unequal variances, the Mann–Whitney U test or Kruskal–Wallis H test were employed. All statistical analyses were performed using GraphPad Prism 8.0 [61]. Statistical significance was set at $P < 0.05$.

Results

Enhancement of targeting ability of MSCs nanovesicles to DCs through P-D2 peptide modification

It has been reported that EVs derived from MSCs have the potential to treat AR by influencing the involvement of DCs [35]. Studies have shown that surface modification with P-D2 peptide can enhance the targeting ability of nanocarriers to DCs [21, 22]. Therefore, we first obtained EVs from MSCs using ultracentrifugation and prepared liposomes containing P-D2 peptide. Subsequently, we loaded P-D2 peptide onto the surface of MSCs-derived EVs using the lipid mixing technique and incubation, resulting in novel MSCs nanovesicles with DCs targeting ability, named P-D2-EVs (Fig. S1A).

Characterization of EVs and P-D2-EVs was performed. Western blot results showed positive expression of extracellular vesicle markers CD9, CD81, CD63, and Alix in both EVs and P-D2-EVs and negative expression of endoplasmic reticulum marker Calnexin (Fig. S1B). TEM revealed that both EVs and P-D2-EVs exhibited a circular shape and had a dual-layered lipid membrane structure (Fig. S1C). NTA demonstrated that the average particle sizes of EVs and P-D2-EVs were 91.97 ± 5.01 nm and 107.82 ± 2.39 nm, respectively (Fig. S1D), with corresponding Zeta potentials of -23.33 ± 1.20 mV and − 16.01 ± 2.08 mV (Fig. S1E). Therefore, both EVs and P-D2-EVs exhibited typical characteristics of EVs. Additionally, after 30 days, the concentration and particle size of P-D2-EVs showed no significant changes, indicating the desired stability of P-D2-EVs (Fig. S1F, G). The loading efficiency of P-D2 peptide on the PS surface was determined to exceed 87% using CBQCA, confirming the stable incorporation of P-D2 peptide at different densities onto the PS surface following size exclusion chromatography purification (Fig. S1H).

To further validate the targeting ability of P-D2-EVs to DCs, we labeled EVs and P-D2-EVs with PKH67 and observed the uptake of these vesicles by DCs at different time points. The results showed that after co-incubation for 2 h, PKH67-EVs and engineered PKH67-P-D2-EVs were internalized by the cells, with stronger fluorescence intensity observed in the PKH67-P-D2-EVs group. Consistent conclusions were drawn after 8 h of co-incubation, and the uptake of PKH67-P-D2-EVs by DCs exhibited a time-dependent pattern (Fig. S1I). This indicates that engineered P-D2-EVs can enhance the targeting ability of EVs to DCs, thereby increasing the uptake of EVs by DCs.

In summary, we successfully prepared novel MSC nanovesicles, P-D2-EVs, with stability and specific targeting effects.

P-D2-EVs are more effective than EVs in treating a mouse model of AR

To investigate the potential of P-D2-EVs in treating AR, we first administered PBS, DiR-labeled EVs, or P-D2-EVs into the nasal cavity of mice induced with ovalbumin (OVA) (Fig. S2A). In vivo, fluorescence imaging and flow cytometry were used to evaluate the biodistribution of EVs or P-D2-EVs in the nasal cavity and their targeting ability towards DCs, respectively. The results of in vivo fluorescence imaging indicated a higher fluorescence signal in the nasal cavity of AR mice administered with P-D2-EVs compared to the Model + DiR-EVs group, suggesting that the modified P-D2-EVs, a novel MSCs nanovesicles, can be delivered more effectively to the AR lesion sites (Fig. S2B). Flow cytometry analysis revealed that MSC-derived EVs targeted only 22% of DCs, whereas P-D2-EVs could target 52.1% of DCs, with a stronger fluorescence intensity of DiR in DCs from the Model + DiR-P-D2-EVs group compared to the EVs group (Fig. S2C). These findings indicate that the novel MSCs nanovesicles, P-D2-EVs, possess specific targeting effects and potential therapeutic efficacy for AR.

To further validate the therapeutic potential of EVs or P-D2-EVs for AR mice, we treated the mice through nasal administration of EVs or P-D2-EVs (Fig. 1A). Compared to the Control group, the Model group exhibited a significant increase in the number of nose-rubbing and sneezing episodes. However, treatment with both types of EVs was able to alleviate nose rubbing and sneezing in AR mice, with the Model + P-D2-EVs group showing a more pronounced inhibitory effect than the Model + EVs group (Fig. 1B).

In addition, the Model group displayed higher total cell count in NALF, serum levels of OVA-specific IgE, and goblet cell percentage compared to the Control group. However, treatment with EVs or P-D2-EVs reversed these effects significantly, with P-D2-EVs showing a more potent reversal effect than EVs (Fig. 1C–E). H&E staining results demonstrated that both EVs and P-D2-EVs significantly improved the number of eosinophils in the OVA-induced nasal mucosa and the increase in nasal mucosa thickness compared to the Model group, indicating that both EVs and P-D2-EVs improved eosinophil infiltration and nasal mucosal hyperplasia, with P-D2-EVs exhibiting a stronger improvement effect (Fig. 1F). Consistently, the treatment with EVs or P-D2-EVs reduced neutrophil infiltration in the nasal mucosa of the Model group, with P-D2-EVs showing a superior inhibitory effect compared to EVs treatment (Fig. 1G).

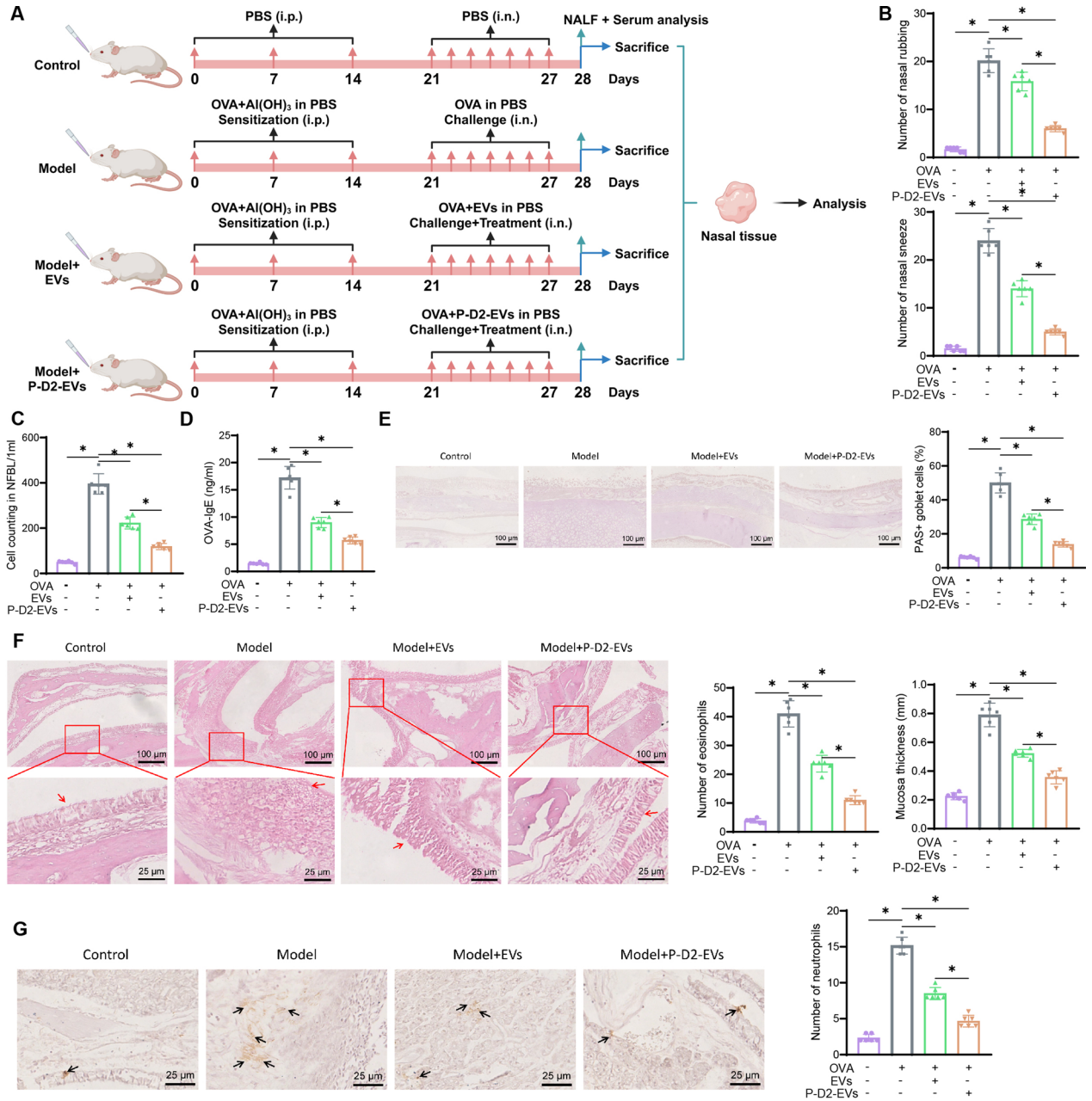

Fig. 1 Therapeutic effects of EVs and P-D2-EVs on AR mice. **A** Flowchart of EVs and P-D2-EVs treatment on AR mice. **B** Number of nose rubbing (itching) and sneezing events of each group of mice (n = 6) within 2 h after the last intranasal OVA administration. **C** Total cell count in NALF of each group of mice (n = 6). **D** OVA-specific serum IgE levels of each group of mice (n = 6). **E** Representative PAS staining images of nasal tissue (scale bar = 100 μm) and quantification of percentage of PAS-positive goblet cells. **F** Representative H&E staining images of nasal tissue (scale bar = 100 μm or 25 μm) and quantification of eosinophils in nasal mucosa and nasal mucosal thickness, red arrows indicate nasal mucosa. **G** Representative images of neutrophil infiltration in nasal mucosa (scale bar = 25 μm) and quantification in each group of mice (n = 6), black arrows indicate positive cells; *NALF* nasal lavage fluid, * represents statistical significance ($P < 0.05$)

These results indicate that we have established a reliable AR mouse model. Both EVs and P-D2-EVs significantly alleviate AR symptoms and inflammation in

Model mice, with the novel MSCs nanovesicles P-D2-EVs exerting a stronger therapeutic effect on AR.

Treatment of AR through regulation of DEGs in DCs by P-D2-EVs

To investigate the mechanism by which the novel MSCs nanovesicles P-D2-EVs improve AR, we collected DCs from mice in the Model group and the Model + P-D2-EVs group using flow cytometry, followed by transcriptome sequencing (Fig. 2A). Transcriptome sequencing results revealed that DCs from the Model group treated with P-D2-EVs showed significant differential expression of 948 genes (differentially expressed genes, DEGs), including 626 upregulated and 322 downregulated genes (Fig. 2B, C). Functional enrichment analysis using the GO and KEGG databases indicated that the DEGs were mainly enriched in several biological processes (BP), such as positive regulation of defense response, cellular components (CC), such as spindle apparatus, and molecular functions (MF), such as cytokine receptor binding (Fig. 2D). Additionally, KEGG enrichment analysis revealed that the DEGs were mainly enriched in signaling pathways, including cytokine-cytokine receptor interaction (Fig. 2E). In conclusion, P-D2-EVs may have therapeutic potential for AR by regulating DEGs in DCs.

Role of DCs in AR revealed by P-D2-EVs through scRNA-seq analysis

Single-cell RNA sequencing (scRNA-seq) can illuminate the transcriptional changes in specific cell subpopulations, aiding in the exploration of key pathways that may influence the occurrence of AR [46]. Therefore, to investigate the impact of P-D2-EVs on the AR process and the role of DCs within it, scRNA-seq was performed on nasal tissue samples collected from three groups of mice: a model group and a model + P-D2-EVs group. The analysis of scRNA-seq data was conducted using the "Seurat" package in the R software (Fig. 2F). After quality control and normalization of the scRNA-seq data, the distribution of cellular RNA was obtained, as shown in Fig. S3A. Subsequently, the correlation coefficients between nCount and percent.mt, as well as between nCount and nFeature, were analyzed, indicating that the filtered cell data had good quality and were suitable for further analysis (Fig. S3B).

Further analysis was carried out on the filtered cells by selecting highly variable genes based on their gene expression variance, resulting in the selection of the top 2000 genes with the highest variance for subsequent analysis (Fig. S3C). Sample cell cycles were calculated using the CellCycleScoring function (Fig. S3D), and preliminary data normalization was performed. Thereafter, principal component analysis (PCA), utilizing the selected highly variable genes, was implemented for linear dimension reduction. A total of 50 principal components were obtained, among which those with smaller P-values and larger standard deviations indicated greater importance (Fig. S3E-F). The results demonstrated that PC_1-PC_30 effectively reflected the information contained in the selected highly variable genes and carried significant analytical significance. Here, we presented the characteristic genes of PC_1 and PC_2 (Fig. S3G), as well as the heatmap of the main correlated gene expressions for PC_1-PC_6 (Fig. S3H).

Moreover, we illustrated the distribution of different sample cells in PC_1 and PC_2 (Fig. S3I), revealing the existence of batch effects between samples. To eliminate these batch effects and improve the accuracy of cell clustering, we employed the harmony package for batch correction of the sample data (Fig. 2G). The results after correction exhibited the successful elimination of batch effects (Fig. 2H).

Subsequently, we employed the UMAP algorithm for non-linear dimension reduction using the first 30 principal components and conducted cluster analysis with a resolution of 0.9 (Fig. S4). Through clustering, we

(See figure on next page.)

Fig. 2 Transcriptome sequencing and biological information analysis of DEGs. **A** Workflow of transcriptome sequencing for mouse DCs in Model group and Model + P-D2-EVs group. **B** Volcano plot of DEGs between mouse DC samples from Model group (n = 3) and Model + P-D2-EVs group (n = 3). **C** Heatmap of DEGs between mouse DC samples from Model group (n = 3) and Model + P-D2-EVs group (n = 3). **D** GO enrichment analysis bubble plot of DEGs. **E** KEGG enrichment analysis bar plot of DEGs. **F** Single-cell sequencing workflow diagram of Model group (n = 3) and Model + P-D2-EVs group (n = 3) mouse nasal tissue samples. **G** Batch correction process diagram of Harmony, with the number of interactions on the x-axis. **H** Distribution of cells in PC_1 and PC_2 after Harmony batch correction, each point represents a cell, different colors represent different samples. **I** UMAP clustering result visualization, two-dimensionally showing the clustering and distribution of cells from Model group (n = 3) and Model + P-D2-EVs group (n = 3) mouse nasal tissue samples, where blue represents samples from the Model group, and red represents samples from the Model + P-D2-EVs group. **J** UMAP clustering result visualization, displaying the clustering and distribution of cells from different sources (n = 3), with each color representing a cluster. **K** Expression levels of known cell lineage-specific marker genes in different clusters, where darker red indicates higher average expression levels and larger circles indicate more cells expressing that gene. **L** Three-dimensional visualization of cell annotations based on UMAP clustering, with each color representing a cell subtype. **M** Visualization of cell annotation results based on UMAP clustering of Model group (n = 3) and Model + P-D2-EVs group (n = 3), where each color represents a cell subtype

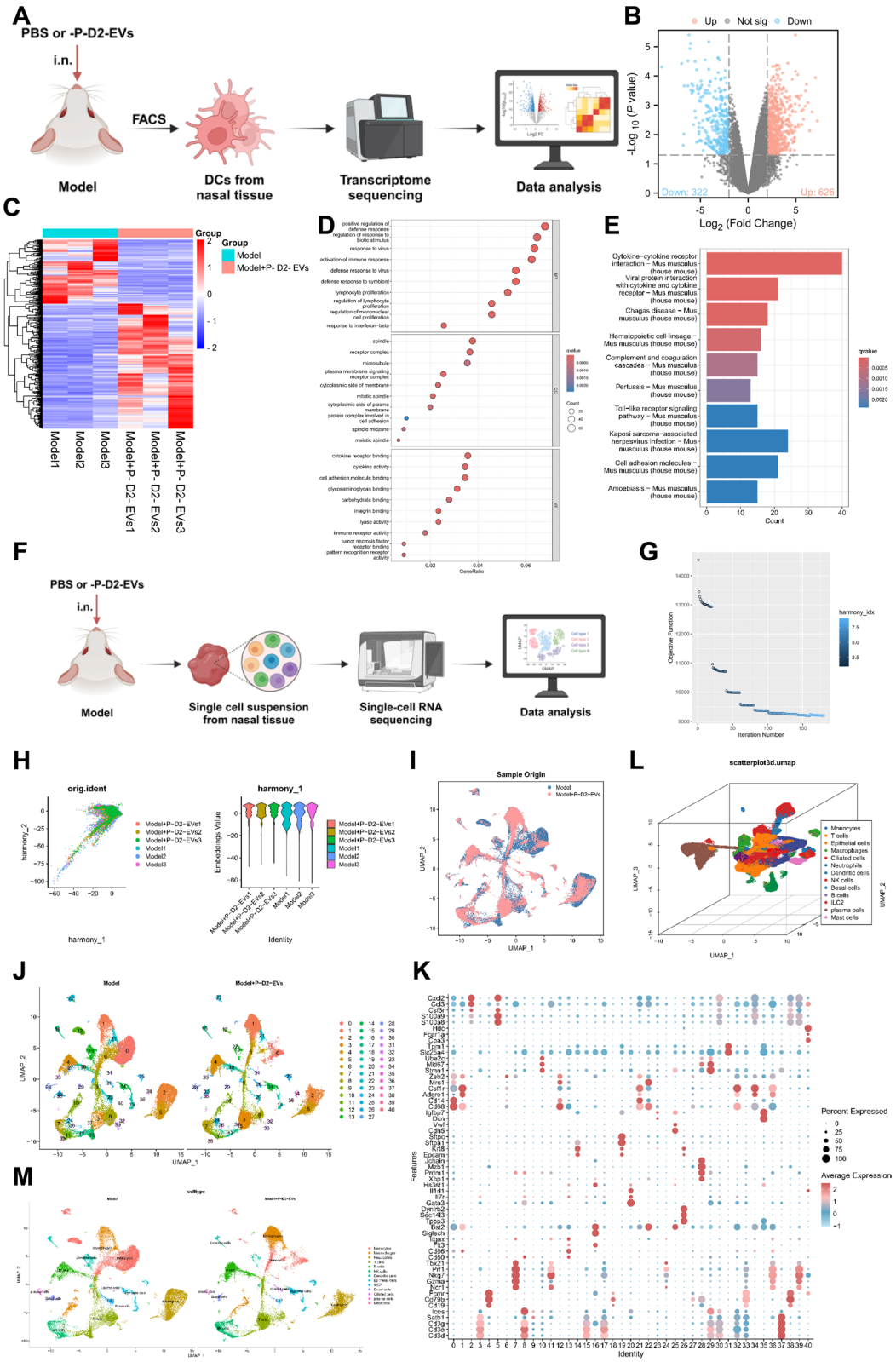

Fig. 2 (See legend on previous page.)

obtained 41 clusters and investigated the marker gene expressions for each cluster (Fig. 2I, J). We then annotated the cells based on known lineage-specific marker genes obtained from relevant literature in combination with the online resource CellMarker (Fig. 2K) [62, 63]. In total, we identified 13 cell categories, including monocytes, macrophages, neutrophils, T cells, B cells, natural killer cells, DCs, epithelial cells, ILC2 (type 2 innate lymphoid cells), basal cells, ciliated cells, plasma cells, and mast cells (Fig. 2L, M).

In summary, the nasal tissue samples from the model and model + P-D2-EVs groups of mice could be classified into 41 clusters comprising 13 distinct cellular subpopulations.

Key mechanisms of P-D2-EVs in suppressing AR through modulating cell interactions

There is increasing evidence suggesting that DCs involved in antigen presentation play a crucial role in allergic diseases, such as AR, and interact with other cells like T cells and ILC2 [35, 64–66]. To investigate whether P-D2-EVs treat AR by influencing DCs, T cells, and ILC2, we first validated the annotation of DCs, T cells, and ILC2 (Fig. S5). Subsequently, using Seurat, we calculated the proportions of different cell types in the Model group and the Model + P-D2-EVs group (Fig. 3A). Compared to the Model group, the Model + P-D2-EVs group exhibited decreased levels of DCs, T cells, and ILC2.

To further validate the specific pathways of P-D2-EVs in treating AR through DCs, T cells, and ILC2, we performed pseudo-time analysis on DC subpopulations using the "monocle" package to construct cell trajectories over time and studied the differences in DCs between pre-and post-treatment with P-D2-EVs. The results revealed that DCs could be divided into three distinct expression patterns or branches based on highly variable genes (Fig. 3B). Visualization using pseudo-time indicated that the trajectory of DCs over time shifted from State 1 to State 3 (Fig. 3C). Furthermore, when displaying cells by different groups, State 1 appeared to be a unique state in the Model + P-D2-EVs group during the recruitment or activation process of DCs (Fig. 3D). Subsequently, we plotted gene expression-pseudo-time curves for marker genes of DCs, which demonstrated a significant decrease in the expression of Igtax (Cd11c), Cd80, and Cd86 in DCs of State 1 along the trajectory over time (Fig. 3E). This suggests that P-D2-EVs may treat AR by inhibiting the recruitment or activation of DCs.

Moreover, we conducted a pseudo-time analysis on T cells. Based on highly variable genes, T cells were divided into five states, with the trajectory of T cells transitioning from State 1 to State 4 (Fig. 3F, G). States 2 and 3 represented specific branches of T cell differentiation in the Model + P-D2-EVs group (Fig. 3H). T cells are typically differentiated into cytotoxic T cells ($CD8^+$T) and helper T cells ($CD4^+$ T), with $CD4^+$ T cells further differentiating into regulatory T cells (Treg), helper T cell 1 (Th1), helper T cell 2 (Th2), and helper T cell 17 (Th17) [67]. Subsequently, we plotted gene expression-pseudo-time curves for marker genes of different T cell subtypes in various differentiation directions. The results revealed a significant decrease in the expression of Th2 cell marker genes Stat6 and Gata3 in States 2 and 3, while the expression of marker genes for $CD8^+$T cells (Cd8a), $CD4^+$ T cells (Cd4), Treg cells (Foxp3, Il2ra also known as Cd25), Th1 cells (Tbx21 also known as T-bet), and Th17 cells (Stat3, Rora) remained relatively stable (Fig. 3I). This suggests that a key mechanism of P-D2-EVs in treating AR may be inhibiting the differentiation of T cells into Th2 cells.

Furthermore, a pseudo-time analysis of ILC2 revealed that they can be classified into five distinct states. The temporal trajectory of their transitions is observed from state 1 to state 3 (Fig. 3J, K). In the process of ILC2 activation, state 1 is a unique branch specific to the Model + P-D2-EVs group (Fig. 3L). Notably, the

(See figure on next page.)

Fig. 3 Pseudotime analysis of DCs and T cell subpopulations. **A** Proportions of different cell subpopulations in different groups (n = 3), represented by different colors. **B** Cell trajectory differentiation diagram for DCs, where different colors represent different states. **C** Pseudotime visualization of DC cell trajectories, with darker colors indicating earlier time points. **D** Cell trajectory visualization of DCs in different groups (n = 3), with different colors representing different groups. **E** Pseudo-temporal expression curves for DC cell marker genes Igtax, Cd80, and Cd86, with time on the x-axis and gene expression levels on the y-axis. **F** Cell trajectory differentiation diagram for T cells, where different colors represent different states. **G** Pseudotime visualization of T cell trajectories, with darker colors indicating earlier time points. **H** Cell trajectory visualization of T cells in different groups (n = 3), with different colors representing different groups. **I** Pseudo-temporal expression curves for marker genes associated with different T cell differentiation directions, with time on the x-axis and gene expression levels on the y-axis. **J** Cell trajectory differentiation map of ILC2, where different colors represent different states. **K** Visualizing the cell trajectory map of ILC2 in pseudo-time, with darker colors indicating earlier time points. **L** Visualization of ILC2 cell trajectories using different grouped samples (n = 3), where different colors represent different groups. **M** Pseudo-time curve of gene expression of Gata3, a marker gene for ILC2 cells, with time on the x-axis and gene expression level on the y-axis. **N** Interaction relationships between cells in the Model group samples (n = 3), with line thickness representing the strength of the interactions. **O** Interaction relationships between cells in the Model + P-D2-EVs group samples (n = 3), with line thickness representing the strength of the interactions

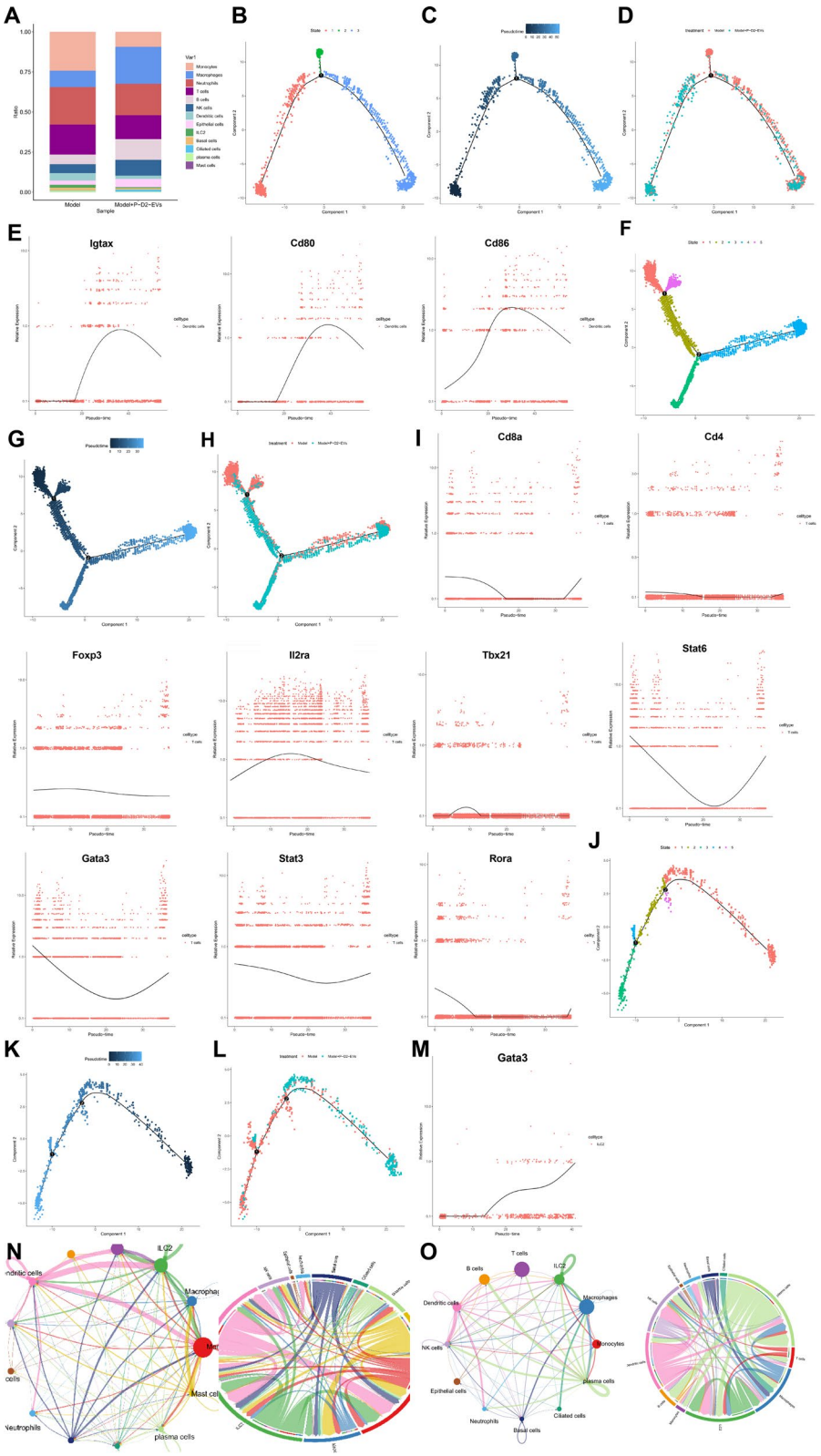

Fig. 3 (See legend on previous page.)

pseudo-time gene expression curve demonstrated that the transcription factor Gata3, a marker of ILC2 activation, exhibits significantly decreased expression in state 1 (Fig. 3M). This indicates a potential role of P-D2-EVs in the therapeutic effect of AR by inhibiting ILC2 activation.

To gain further insight into the regulatory mechanisms underlying the therapeutic effect of P-D2-EVs on AR, we employed the "CellChat" package to investigate the cellular communication between DCs, T cells, and ILC2 cells. The results revealed reduced interactions between DCs and T cells, as well as between T cells and ILC2 cells in the Model + P-D2-EVs group nasal tissue compared to the Model group nasal tissue (Fig. 3N, O). This suggests that P-D2-EVs treatment weakens the cellular communication between DCs and T cells, as well as between T cells and ILC2.

Taken together, these findings indicate that the key regulatory mechanism of P-D2-EVs in treating AR is likely associated with the inhibition of DC recruitment and activation, which in turn affects their function and weakens their crosstalk with T cells, ultimately leading to the suppression of Th2 differentiation and the subsequent inhibition of ILC2 activation.

P-D2-EVs crucially regulate DC function in the treatment of AR via Fut1

To further investigate the specific mechanism of P-D2-EVs in treating AR, we performed differential analysis on the DCs subpopulation from single-cell RNA sequencing data and identified 335 differentially expressed genes (ScRNA-DEGs), with 159 genes upregulated and 176 genes downregulated (Fig. S6A). Venn diagram analysis revealed 27 overlapping genes between ScRNA-DEGs and differentially expressed genes (DEGs) from transcriptomic analysis (Fig. S6B). Subsequently, we extracted 9 commonly differentially expressed genes (B-DEGs) from the intersection of genes that are either upregulated or downregulated in both single-cell and transcriptomic data. Among them, 6 genes (Mrc1, Cdh1, Clec10a, Scimp, Ckb, Gsn) showed high expression at both levels, while 3 genes (Hopx, Kdr, Fut1) showed low expression (Fig. S6C, D).

Further examination of the differential expression pattern of B-DEGs revealed that Fut1 exhibited the most significant differential expression at both single-cell and transcriptomic levels (Fig. S6E, F). GO enrichment analysis indicated that B-DEGs were primarily enriched in biological processes such as trophectodermal cell differentiation, cellular components like myelin sheath, and molecular functions, including cadherin binding (Fig. S6G). Additionally, KEGG enrichment analysis revealed that B-DEGs were mainly enriched in the Rap1 signaling pathway, whereas Fut1 was primarily involved in signaling pathways such as Glycosphingolipid biosynthesis—globo and isoglobo series (Fig. S6H).

In summary, these results demonstrate that Fut1 may serve as a key gene regulating the functionality of DCs in the process of P-D2-EVs treatment for AR, potentially exerting its effects through involvement in glycosylation.

P-D2-EVs regulate the activation and differentiation of DCs by inhibiting Fut1

The results of our bioinformatics analysis suggest that P-D2-EVs may play a crucial role in AR therapy by modulating the activation of DCs. Fut1 is a key factor that affects the functionality of DCs. To validate this conclusion further, we first used flow cytometry to detect the percentage of DCs in nasal tissues of control mice, model mice, and model mice treated with P-D2-EVs. The results showed that the proportion of DCs in the model mice treated with P-D2-EVs was restored compared to the model mice (Fig. 4A). Subsequently, further flow cytometry analysis revealed that the proportion of Ki67-positive cells in DCs of the nasal tissues of model mice was significantly increased compared to the control group, which was reversed by P-D2-EVs treatment in model mice (Fig. 4B). This result is consistent with the expression level of Ki67 mRNA in DCs detected by RT-qPCR (Fig. 4C). These results suggest that P-D2-EVs inhibit the recruitment and activation of DCs in AR mice nasal tissues.

Next, we conducted RT-qPCR and Western blot analysis on sorted nasal tissue DCs. The results showed that compared to the control group, the mRNA and protein expression of Fut1 in DCs of the model group were significantly upregulated, which was effectively reversed by P-D2-EVs treatment (Fig. 4D, E). This further validates that Fut1 is a key factor regulated by P-D2-EVs in modulating the functionality of DCs.

To further investigate the impact of P-D2-EVs on DCs, we extracted mouse bone marrow cells and induced their differentiation into immature iDCs with the addition or absence of P-D2-EVs, GM-CSF, and IL-4 (Fig. S7A). Flow cytometry analysis revealed that in the iDCs group, P-D2-EVs treatment inhibited the increase in the mean fluorescence intensity of surface markers CD86, CD80, MHC-II, and CD11c induced by GM-CSF and IL-4 (Fig. S7B). This suggests that P-D2-EVs suppress the differentiation of DCs.

To further study the effect of P-D2-EVs on the maturation of DCs, we added or did not add P-D2-EVs to the differentiation of mouse bone marrow cells into iDCs induced by GM-CSF and IL-4 and further induced their differentiation into mature dendritic cells (mDCs) with the addition of LPS (Fig. S7C). Flow cytometry results showed that the addition of P-D2-EVs did not affect the

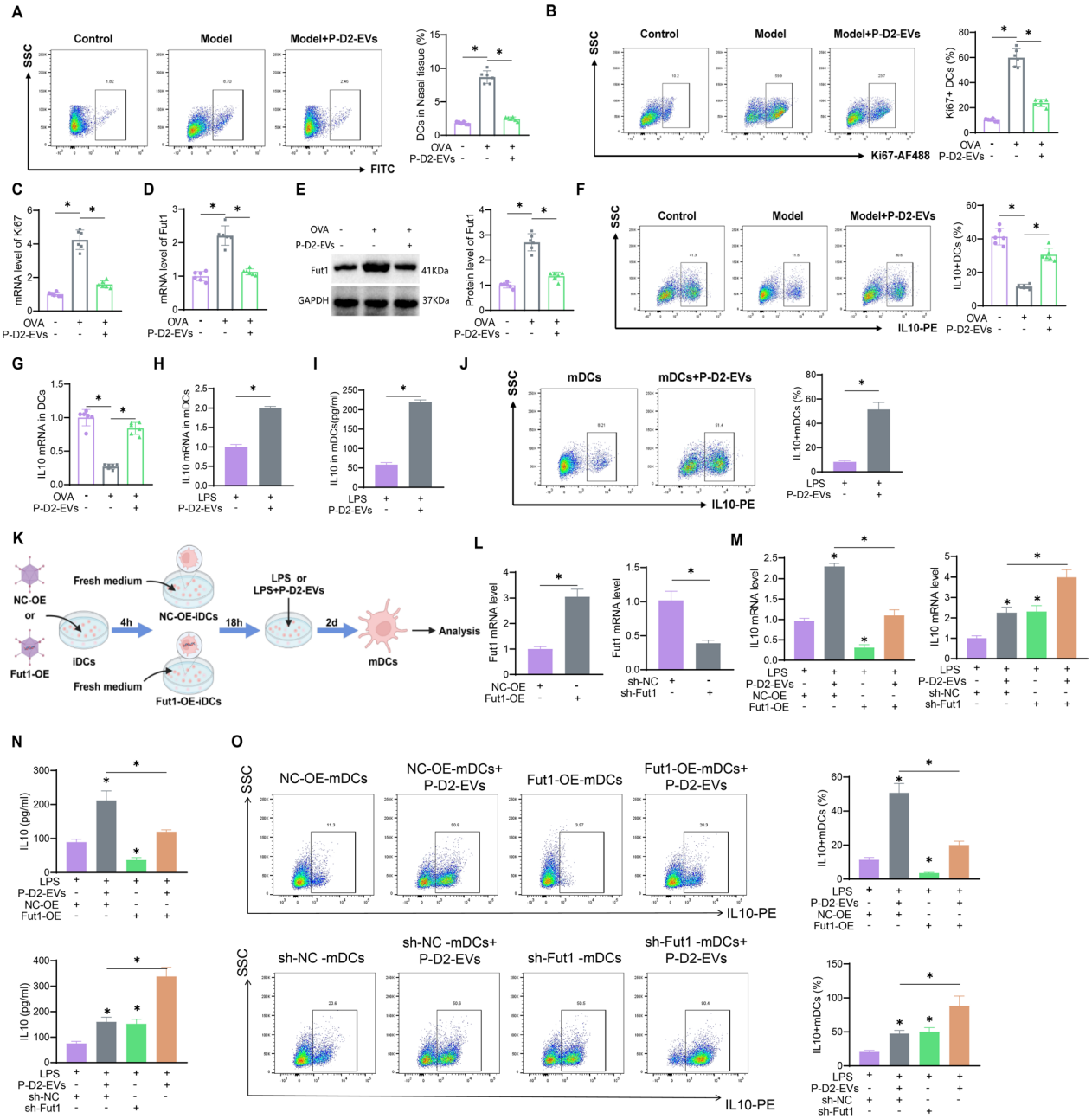

Fig. 4 The impact of P-D2-EVs on DCs activation and metabolism through the regulation of Fut1. **A** Flow cytometric analysis of the percentage of DCs in nasal tissue of each mouse group (n = 6). **B** Flow cytometric analysis of the percentage of Ki67-positive cells in DCs of each mouse group (n = 6). **C** RT-qPCR analysis of Ki67 mRNA expression in DCs of different mouse groups (n = 6). **D** RT-qPCR analysis of Fut1 mRNA expression in DCs of different mouse groups (n = 6). **E** Western blot analysis of Fut1 protein expression in DCs of different mouse groups (n = 6). **F** Flow cytometric analysis of the percentage of IL10-positive cells in DCs of each mouse group (n = 6). **G** RT-qPCR analysis of IL10 mRNA expression in DCs of different mouse groups (n = 6). **H** RT-qPCR analysis of IL10 mRNA expression in different treated mDCs. **I** ELISA analysis of IL10 levels in the supernatant of different treated mDCs. **J** Flow cytometric analysis of intracellular IL-10 levels in different treated mDCs. **K** The schematic diagram illustrates the treatment methods of NC-OE-mDCs, Fut1-OE-mDCs, NC-OE-mDCs + P-D2-EVs, and Fut1-OE-mDCs + P-D2-EVs, as well as sh-NC-mDCs, sh-Fut1-mDCs, sh-NC-mDCs + P-D2-EVs, and sh-Fut1-mDCs + P-D2-EVs. **L** Detection of Fut1 overexpression efficiency in iDCs using RT-qPCR. **M** Detection of IL10 mRNA expression in mDCs from different treatment groups using RT-qPCR. **N** Analysis of IL10 levels in the supernatant of mDCs from different treatment groups through ELISA. **O** Analysis of intracellular IL-10 levels in mDCs from different treatment groups using flow cytometry

expression of surface markers in mDCs compared to the mDCs group (Fig. S7D). This indicates that P-D2-EVs do not affect the mature phenotype of DCs.

Research has shown a close correlation between the induction of IL10 secretion by DCs and the inhibition of Th2 immune response in T cells [38]. Therefore, to investigate the impact of P-D2-EVs on IL10 metabolism in DCs, we conducted flow cytometry analysis and found a significant decrease in the percentage of IL10-positive cells in the nasal tissue of Model mice compared to the Control group. However, treatment with P-D2-EVs in Model mice appeared to reverse this phenomenon (Fig. 4F). RT-qPCR analysis of IL10 expression in DCs of different groups of mice revealed that P-D2-EVs significantly blocked the mRNA expression suppression of IL10 induced by OVA in AR mice (Fig. 4G). In addition, in vitro cell experiments confirmed that the mRNA expression of IL10 was significantly upregulated in the P-D2-EVs + mDCs group compared to the mDCs group (Fig. 4H). Furthermore, ELISA and flow cytometry confirmed the induction of IL10 production in mDCs treated with P-D2-EVs, both in the cell supernatant and intracellularly (Fig. 4I, J).

To further explore the relationship between Fut1 expression and the regulation of DCs metabolic function by P-D2-EVs, we prepared adenoviral vectors overexpressing Fut1 (Fut1-OE) and empty adenoviral vectors (NC-OE), which were transfected into iDCs and then co-induced with LPS with or without the addition of P-D2-EVs to induce iDC maturation (Fig. 4K). The efficiency of Fut1 overexpression was validated (Fig. 4L). RT-qPCR analysis revealed that Fut1 overexpression in the Fut1-OE-mDCs + P-D2-EVs group reversed the upregulation of IL10 mRNA expression in mDCs treated with P-D2-EVs compared to the NC-OE-mDCs + P-D2-EVs group (Fig. 4M. Moreover, the results of ELISA and flow cytometry detecting IL10 levels in the cell supernatant and intracellularly were consistent with this finding (Fig. 4N, O). This suggests that Fut1 is a key gene involved in the regulation of IL10 expression in DCs by P-D2-EVs.

In summary, P-D2-EVs reshape the metabolic function of DCs by inhibiting Fut1 expression and promoting IL10 expression, while overexpression of Fut1 can counteract this process.

P-D2-EVs modulate α-(1,2)-fucosylation of ICAM1 to downregulate DCs inhibition

DCs are capable of antigen presentation and formation of cell clusters with T cells, thereby activating T cells. This process is closely related to the adhesion molecule ICAM1 on DCs [68, 69]. Glycosylation of ICAM1 is also crucial for cell adhesion in inflammatory responses [70–73]. Fucosylation is one of the most important types of glycosylation and serves as a post-translational modification for polysaccharides, proteins, and lipids. A study found that Fut1, as an α-(1,2)-fucosyltransferase, can promote ICAM1 fucosylation and impact cell adhesion [52]. However, the role of Fut1 in the regulation of DCs function through fucosylation of ICAM1 and its involvement in the regulation of Th2 differentiation of T cells remains unclear.

To further investigate the specific mechanism of P-D2-EVs in reshaping DCs metabolism through the mediation of Fut1, we first conducted Western blot analysis of α-(1,2)-fucosylated protein enriched with Ulex European Agglutinin 1 (UEA1) in differently treated mDCs (Fig. 5A). Western blot analysis of α-(1,2)-fucosylated ICAM1 in mDCs showed that compared to the mDCs group, the P-D2-EVs + mDCs group exhibited a decrease in the total protein input of Fut1, while the total protein input of ICAM1 did not show a significant difference. However, the α-(1,2)-fucosylation of ICAM1 was significantly reduced in the P-D2-EVs + mDCs group (Fig. 5B). Immunoprecipitation (IP) of ICAM1, followed by Western blot analysis with UEA1, demonstrated a reduction in the binding between UEA1 and ICAM1 in mDCs treated with P-D2-EVs (Fig. 5C). Moreover, fluorescence co-localization analysis of ICAM1 and UEA1 revealed that the fluorescence intensity of co-localized UEA1 and ICAM1 (yellow color) was significantly lower in the

(See figure on next page.)

Fig. 5 Influence of P-D2-EVs on Fut1-mediated fucosylation of ICAM1. **A** Western blot analysis of UEA-1-enriched mDCs under different treatments. **B** Western blot analysis and quantification of α-(1,2)-fucosylation status of ICAM1 protein in each group after UEA-1 enrichment. **C** IP-based detection and quantification of ICAM1 binding to UEA1 in each group. **D** Immunofluorescence co-localization (yellow) and quantification of UEA1 and ICAM1, with DAP(I) staining the cell nucleus in blue, scale bar = 25 μm. **E** Western blot analysis and quantification of α-(1,2)-fucosylation status of ICAM1 protein in each group after UEA-1 enrichment. **F** IP-based detection and quantification of ICAM1 binding to UEA1 in each group. **G** Immunofluorescence co-localization (yellow) and quantification of UEA1 and ICAM1, with DAP(I) staining the cell nucleus in blue, scale bar = 25 μm. **H** Schematic representation of Fut1-OE-iDCs treated with 2DGal; (I) Western blot analysis and quantification of α-(1,2)-fucosylation status of ICAM1 protein in each group after UEA-1 enrichment. **J** IP-based detection and quantification of ICAM1 binding to UEA1 in each group. **K** Immunofluorescence co-localization (yellow) and quantification of UEA1 and ICAM1, with DAP(I) staining the cell nucleus in blue, scale bar = 25 μm; UEA1: Ulex europaeus agglutinin 1, 2DGal: 2-deoxy-D-galactose. * indicates statistical significance compared to the control group or between two groups, with $P < 0.05$; all experiments were repeated three times

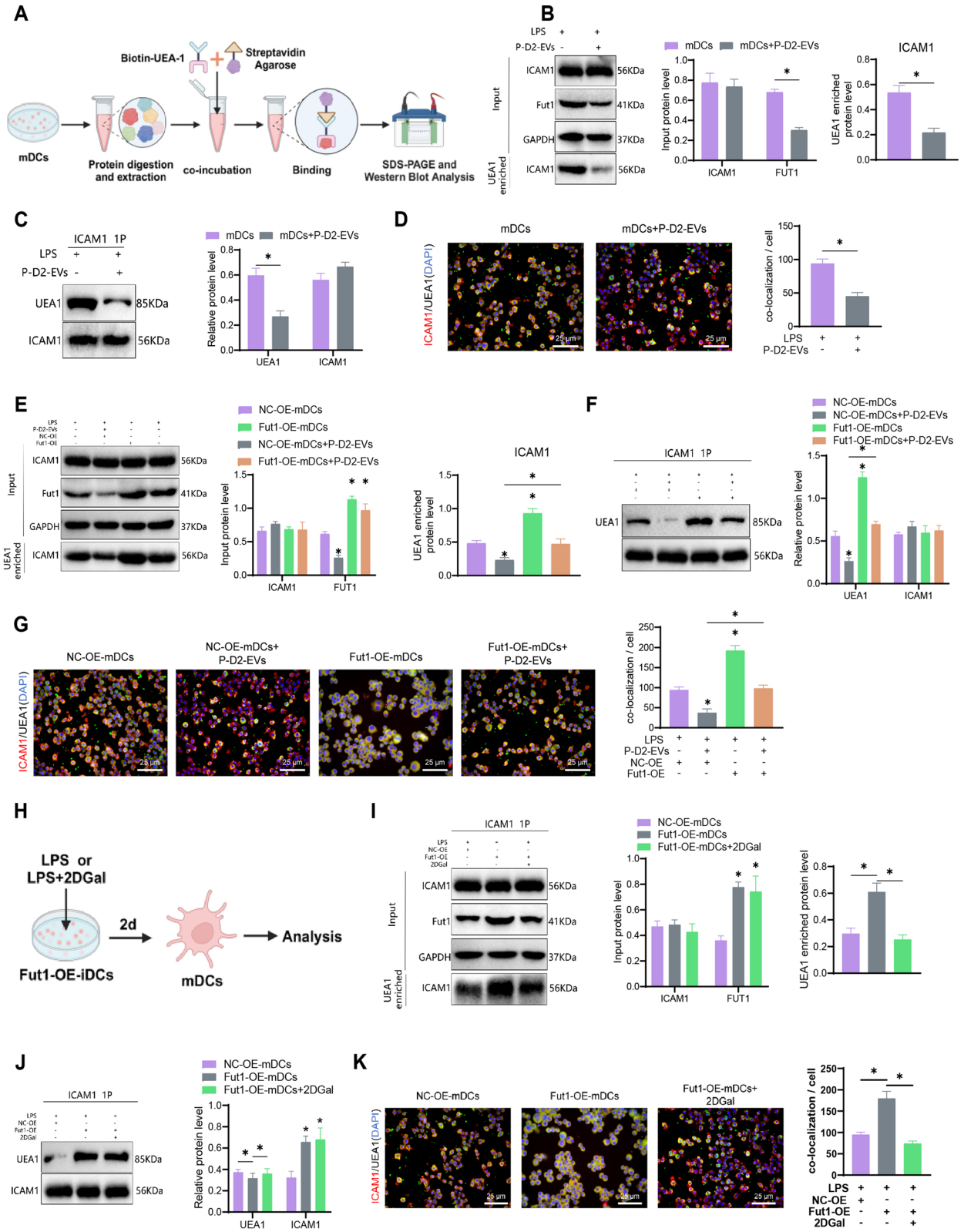

Fig. 5 (See legend on previous page.)

P-D2-EVs + mDCs group compared to the mDCs group (Fig. 5D). These results suggest that P-D2-EVs can inhibit α-(1,2)-fucosylation of ICAM1 in DCs.

To investigate the role of P-D2-EVs in regulating ICAM1 fucosylation through Fut1 further, Western blot analysis was performed using UEA-1-enriched samples. The results revealed that the overexpression of Fut1 in Fut1-OE-mDCs + P-D2-EVs reversed the inhibitory effect of P-D2-EVs treatment on the α-(1,2)-fucosylation of ICAM1 (Fig. 5E). Furthermore, immunoprecipitation (IP) assays demonstrated that Fut1 overexpression restored the protein binding of UEA1 and ICAM1, which had been reduced by P-D2-EVs treatment in the NC-OE-mDCs + P-D2-EVs group (Fig. 5F). Consistent with these findings, fluorescence co-localization of UEA1 and ICAM1 confirmed the same conclusion (Fig. 5G). These results indicate that Fut1 overexpression counteracts the inhibitory effect of P-D2-EVs on the α-(1,2)-fucosylation of ICAM1 in DCs.

To further validate the regulatory effect of Fut1 on ICAM1 fucosylation, we induced the maturation of iDCs by co-treating with the α-(1,2)-fucosylation inhibitor, 2-deoxy-D-galactose (2DGal), and LPS (Fig. 5H). We found that the addition of 2DGal could counteract the upregulation of α-(1,2)-fucosylation of ICAM1 mediated by Fut1 overexpression in Fut1-OE-mDCs, restoring the binding and fluorescence co-localization of UEA1 and ICAM1 (Fig. 5I–K. Importantly, the presence of 2DGal did not affect the total protein expression of Fut1 in the Fut1-OE-mDCs + 2DGal group (Fig. 5I).

Taken together, these findings demonstrate that P-D2-EVs exert their inhibitory effect on the α-(1,2)-fucosylation of ICAM1 in DCs by downregulating the expression of Fut1.

P-D2-EVs inhibit activation of the P38 MAPK signaling pathway by modulating ICAM1 alginate glycosylation

The inactivation of the P38 MAPK signaling pathway can regulate the metabolism of DCs and block the activation of T cells [74]. To further investigate whether P-D2-EVs can inhibit the activation of the P38 MAPK signaling pathway by mediating the inhibition of ICAM1 alginate glycosylation through Fut1, we first examined the regulatory effect of P-D2-EVs on the P38 MAPK signaling pathway. Western blot analysis revealed that treatment with P-D2-EVs downregulated the ratio of phosphorylated P38 (p-P38) to P38 compared to the NC-OE-mDCs group, while overexpression of Fut1 reversed the inhibitory effect of P-D2-EVs on p-P38/P38 (Fig. 6A). This indicates that overexpression of Fut1 significantly restores the inhibitory effect of P-D2-EVs on the activation of the P38 MAPK pathway. Furthermore, in comparison to the Fut1-OE-mDCs group, treatment with 2DGal, an inhibitor of ICAM1 α-(1,2)-alginate glycosylation, reversed the increase in p-P38/P38 ratio caused by Fut1 overexpression (Fig. 6B). This suggests that Fut1 activates the P38 MAPK pathway by promoting ICAM1 α-(1,2)-alginate glycosylation.

To further investigate whether P-D2-EVs regulate DC metabolism by mediating the influence of Fut1 on ICAM1 alginate glycosylation, RT-qPCR revealed that the use of 2DGal on the basis of Fut1 overexpression significantly restored the downregulation of IL10 mRNA expression caused by Fut1 overexpression (Fig. 6C). Additionally, ELISA and flow cytometry confirmed that 2DGal treatment reversed the inhibitory effect of Fut1-OE-mDCs on IL10 production, both in the culture supernatant and intracellularly (Fig. 6D, E). These results indicate that P-D2-EVs reshape the metabolism of DCs by downregulating the expression of Fut1 and inhibiting ICAM1 alginate glycosylation.

To further validate the correlation between the P38 MAPK signaling pathway and ICAM1-mediated regulation of DC metabolism, we conducted a rescue experiment of the P38 MAPK pathway using the P38 MAPK activator Anisomycin (Fig. 6F). Western blot analysis showed that Anisomycin treatment in the mDCs + 2DGal + Anisomycin group blocked the inhibitory effect of 2DGal, an inhibitor of ICAM1 α-(1,2)-alginate glycosylation, on the P38 MAPK pathway (Fig. 6G). RT-qPCR results indicated that the use of Anisomycin in the mDCs + 2DGal + Anisomycin group restored the upregulation of IL10 mRNA expression caused by 2DGal treatment (Fig. 6H). Moreover, ELISA and flow cytometry analysis yielded consistent results regarding the levels of IL10 in the culture supernatant and intracellularly (Fig. 6I, J). This validates that the activation of the P38 MAPK pathway reverses the inhibitory effects of ICAM1 alginate glycosylation on the reshaping of IL10 metabolism.

These findings demonstrate that P-D2-EVs inhibit the activation of the P38 MAPK signaling pathway by downregulating Fut1 expression and inhibiting ICAM1 α-(1,2)-alginate glycosylation, ultimately improving the metabolic function of DCs regarding IL10.

P-D2-EVs suppress Th2 differentiation by inhibiting the Fut1/ICAM1/P38 MAPK pathway in DCs

To investigate the impact of P-D2-EVs on the priming capacity of mDCs for Th2 immune response further, co-culture experiments were conducted between mDCs and $CD4^+$ T cells (Fig. 7A). IL-4 is a hallmark secretion factor of Th2 cells, while GATA3 serves as a marker gene for Th2 differentiation [75]. Flow cytometry results revealed that co-culture of mDCs with $CD4^+$ T cells significantly increased the percentages

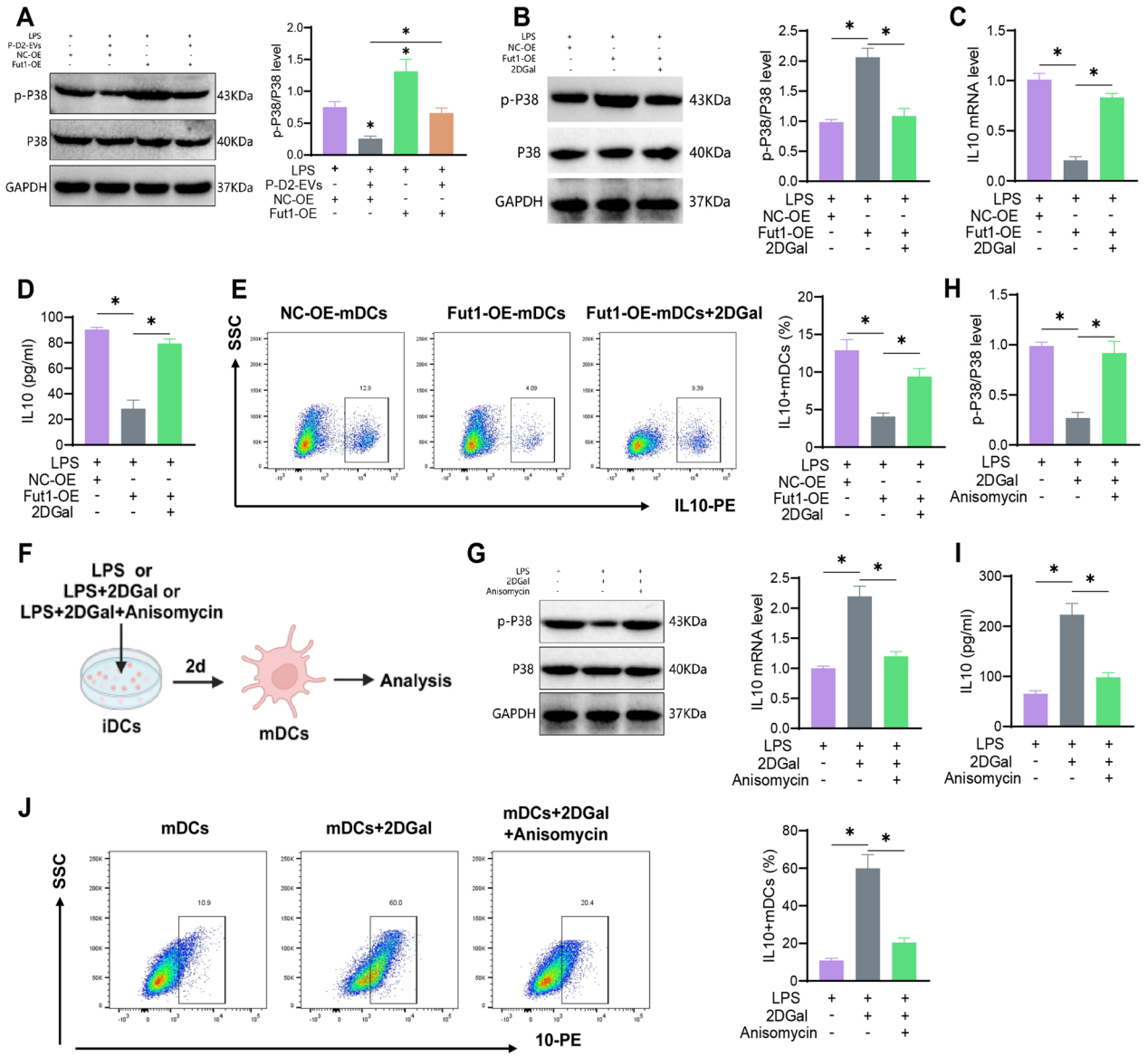

Fig. 6 Influence of P-D2-EVs on DC metabolism via the Fut1/ICAM1/P38 MAPK pathway. **A**, **B** Quantification of p-P38 and P38 expression, as well as the p-P38/P38 ratio, in mDCs from different treatment groups using Western blot. **C** mRNA expression of IL10 in mDCs from different treatment groups measured by RT-qPCR. **D** Levels of IL10 in the supernatant of mDCs from different treatment groups analyzed using ELISA. **E** Analysis of intracellular IL-10 levels in mDCs from different treatment groups using flow cytometry. **F** Schematic representation of the culture conditions for mDCs, mDCs + 2DGal, and m + 2DGal + Anisomycin groups. **G** Quantification of p-P38 and P38 expression, as well as the p-P38/P38 ratio, in mDCs from different treatment groups using Western blot. **H** mRNA expression of IL10 in mDCs from different treatment groups measured by RT-qPCR. **I** Levels of IL10 in the supernatant of mDCs from different treatment groups analyzed using ELISA. **J** Analysis of intracellular IL-10 levels in mDCs from different treatment groups using flow cytometry; 2DGal: 2-deoxy-D-galactose; *indicates statistical significance compared to the control group or between two groups, with $P < 0.05$; all experiments were repeated three times

of IL-4 and GATA3 in $CD4^+$ T cells, compared to the $CD4^+$ T cell-only group. However, the co-culture of P-D2-EV-treated mDCs (P-D2-EV-mDCs) with $CD4^+$ T cells reversed this phenomenon (Fig. 7B). RT-qPCR analysis of mRNA expression in $CD4^+$ T cells after co-culture showed consistent results with flow cytometry (Fig. 7C). Furthermore, ELISA measurement of IL-4 levels in the supernatant after co-culture demonstrated that P-D2-EV-treated mDCs impeded the upregulation of IL-4 by mDCs (Fig. 7D). These findings suggest that LPS-induced mature mDCs promote $CD4^+$ T cell differentiation towards Th2 cells, whereas P-D2-EVs

treatment inhibits the priming capacity of mDCs for Th2 differentiation.

Subsequently, to investigate whether P-D2-EVs modulate Th2 differentiation through the Fut1/ICAM1/P38 MAPK pathway in DCs, flow cytometry analysis of co-cultured $CD4^+$ T cells was performed. It was discovered that co-culture of P-D2-EV-treated mDCs overexpressing Fut1 (P-D2-EV-Fut1-OE-mDCs) with $CD4^+$ T cells restored the percentages and mRNA expression of IL-4 and GATA3 in $CD4^+$ T cells, compared to the $CD4^+$ T cells co-cultured with P-D2-EV-negative control overexpressing mDCs (Fig. 7E, F). Additionally, ELISA analysis of the supernatant from the co-culture showed that Fut1 overexpression prevented the inhibitory effect of P-D2-EV-treated mDCs on IL-4 secretion (Fig. 7G). These results indicate that P-D2-EVs suppress Th2 differentiation by inhibiting the Fut1/ICAM1/P38 MAPK pathway in DCs.

In order to further investigate the correlation between P-D2-EVs and the remodeling of DCs through the Fut1/ICAM1/P38 MAPK pathway in the suppression of IL10 metabolism and Th2 differentiation, $CD4^+$ T cells were pre-treated with IL10 receptor IL10Rα blocking antibody (Fig. 7H). The detection results of Th2 differentiation-related indicators indicated that, compared to the $CD4^+$ T + mDCs group, mDCs treated with P-D2-EVs exhibited impaired promotion of IL4 and GATA3 percentages and mRNA expression in $CD4^+$ T cells, as well as IL4 levels in the co-culture supernatant. However, this phenomenon was reversed when $CD4^+$ T cells were subsequently treated with IL10Rα antibody (Fig. 7I–K). To further verify that P-D2-EVs mediated the suppression of Th2 differentiation through upregulating DCs IL10 metabolism, co-culture experiments were conducted with mDCs and $CD4^+$ T cells using IL10 antibody (Fig. 7L). The results were consistent with those of IL10Rα antibody treatment (Fig. 7M–O). Subsequently, further regulatory mechanism verification was performed through co-culture experiments with IL10 and mDCs plus $CD4^+$ T cells (Fig. 7P). It was found that IL10 treatment could restore the percentages and mRNA expression of IL4 and GATA3 in $CD4^+$ T cells, as well as the IL4 levels in the co-culture supernatant affected by Fut1 overexpression in DCs (Fig. 7Q–S). These results indicate that P-D2-EVs reshape DCs' IL10 metabolism to suppress Th2 differentiation by regulating the Fut1/ICAM1/P38 MAPK pathway.

To further verify the inhibitory effect of P-D2-EVs on Th2 differentiation, Th2 cells in mouse nasal tissues were sorted using the strategy shown in Fig. S8A. Flow cytometry was performed to detect the percentages of Th2 cells in $CD4^+$ T cells of the Control group, Model group, and Model + P-D2-EVs group. It was found that compared to the Model group, the Model + P-D2-EVs group showed significant restoration of the increased proportion of Th2 cells in AR model mice after P-D2-EVs treatment (Fig. S8B). Subsequently, further flow cytometry analysis revealed that compared to the control group, the proportion of GATA3-positive cells in Th2 cells of model mice nasal tissues significantly increased, while this condition was reversed when P-D2-EVs were used to treat model mice (Fig. S8C). RT-qPCR was used to detect the mRNA expression of IL4 and GATA3 in Th2 cells, further confirming the inhibitory effect of P-D2-EVs on Th2 differentiation in AR model mice (Fig. S8D). These results indicate that

(See figure on next page.)

Fig. 7 The impact of P-D2-EVs on regulating the Fut1/ICAM1/P38 MAPK pathway and IL10 metabolism in DCs on Th2 differentiation. **A** Schematic representation of co-culturing mDCs with $CD4^+$ T cells. **B** Flow cytometric analysis of the percentage of IL4 and GATA3 in mDCs co-cultured with $CD4^+$ T cells under different treatments. **C** RT-qPCR analysis of mRNA expression levels of IL4 and GATA3 in mDCs co-cultured with $CD4^+$ T cells under different treatments. **D** ELISA analysis of IL4 levels in the supernatant of mDCs co-cultured with $CD4^+$ T cells under different treatments. **E** Flow cytometric analysis of the percentage of IL4 and GATA3 in mDCs co-cultured with $CD4^+$ T cells under different treatments. **F** RT-qPCR analysis of mRNA expression levels of IL4 and GATA3 in mDCs co-cultured with $CD4^+$ T cells under different treatments. **G** ELISA analysis of IL4 levels in the supernatant of mDCs co-cultured with $CD4^+$ T cells under different treatments; * indicates statistical significance compared to the control group or between two groups ($P < 0.05$); all experiments repeated three times. **H** Schematic diagram of co-culture of CD4 + T cells with mDCs after IL10 receptor blockade. **I** Flow cytometry analysis of the percentage of intracellular IL4 and GATA3 in CD4 + T cells co-cultured with mDCs under different treatments. **J** RT-qPCR detection of mRNA expression levels of IL4 and GATA3 in CD4 + T cells co-cultured with mDCs under different treatments. **K** ELISA analysis of the level of IL4 in the supernatant of co-cultures of mDCs and CD4 + T cells under different treatments. **L** Schematic diagram of co-culture of CD4 + T cells and mDCs with IL10 antibody. **M** Flow cytometry analysis of the percentage of intracellular IL4 and GATA3 in CD4 + T cells co-cultured with mDCs and IL10 antibody under different treatments; (N) RT-qPCR detection of mRNA expression levels of IL4 and GATA3 in CD4 + T cells co-cultured with mDCs and IL10 antibody under different treatments. **O** ELISA analysis of the level of IL4 in the supernatant of co-cultures of mDCs and CD4 + T cells with IL10 antibody. **P** Schematic diagram of co-culture of CD4 + T cells and mDCs with IL10. **Q** Flow cytometry analysis of the percentage of intracellular IL4 and GATA3 in CD4 + T cells co-cultured with mDCs and IL10 under different treatments. **R** RT-qPCR detection of mRNA expression levels of IL4 and GATA3 in CD4 + T cells co-cultured with mDCs and IL10 under different treatments. **S** ELISA analysis of the level of IL4 in the supernatant of co-cultures of mDCs and CD4 + T cells with IL10; *indicates a significant difference between two groups with $P < 0.05$, all experiments were repeated three times

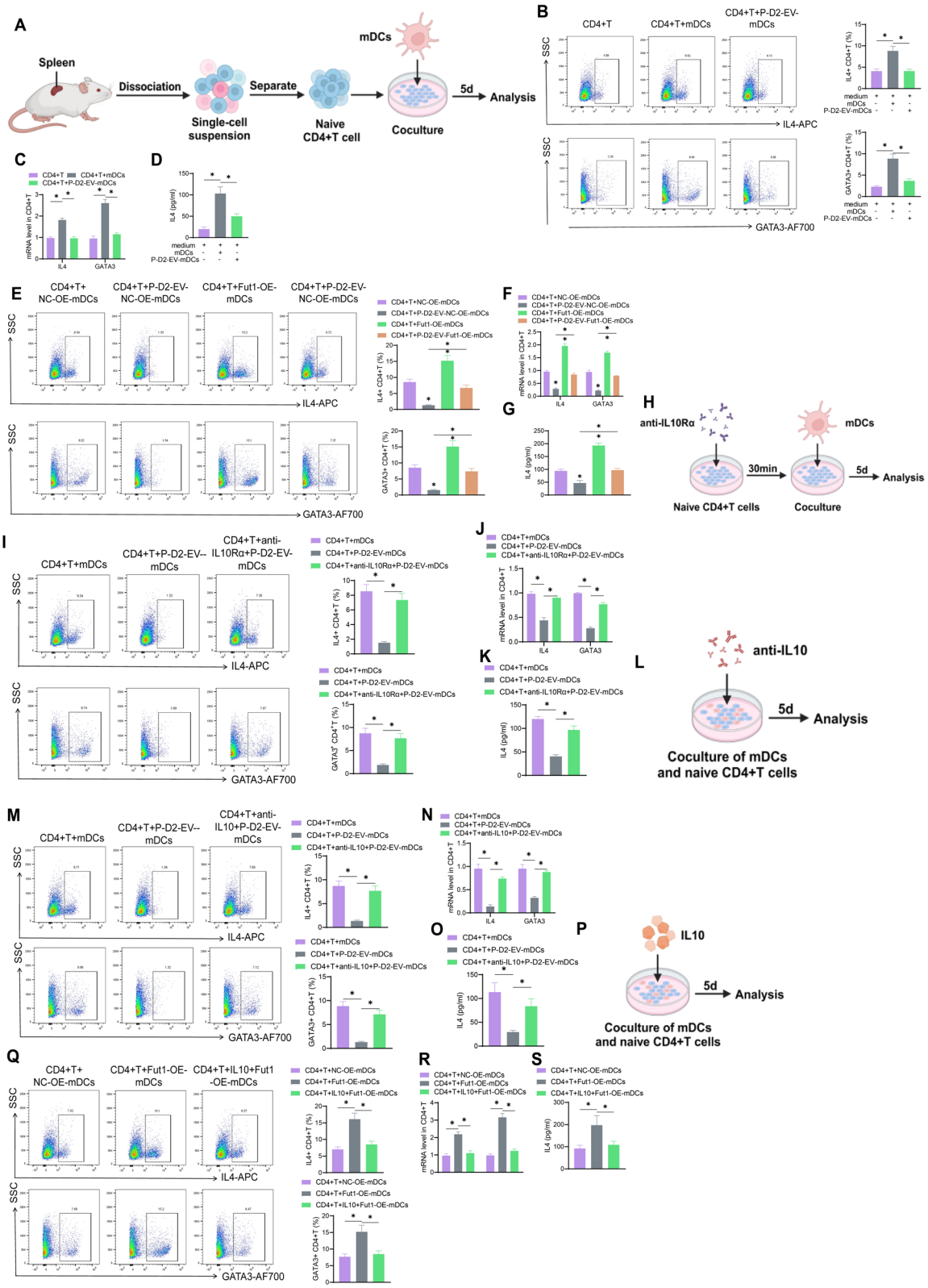

Fig. 7 (See legend on previous page.)

P-D2-EVs inhibit the differentiation and activation of Th2 cells in AR mice.

In conclusion, P-D2-EVs inhibit Th2 differentiation in AR mice by suppressing the activation of the Fut1/ICAM1/P38 MAPK pathway, promoting DCs' IL10 metabolism.

The impact of P-D2-EVs on ILC2 activation through the mediation of DCs-mediated Th2 differentiation

There is a close cellular crosstalk between Th2 cells and ILC2 cells, and the activation of ILC2 cells is closely related to the pathogenesis of allergic inflammation [75, 76]. Therefore, we further investigated the influence of P-D2-EVs on ILC2 activation through the mediation of DCs-mediated Th2 differentiation.

Initially, ILC2 cells were isolated from the nasal-associated lymphoid tissue (NALT) of mice and co-cultured with mDCs and $CD4^+$ T cells in the conditioned medium (Fig. 8A). Induction and blockade experiments were conducted by pre-treating with an anti-IL4Rα antibody or adding IL4 and IL4 antibodies during co-culture (Fig. 8B, C). IL-13 and IL-5 are secretion factors characteristic of ILC2, with GATA3 serving as a key gene marker for ILC2 activation [75]. Analysis through flow cytometry and RT-qPCR revealed that, compared to co-cultures of ILC2 and $CD4^+$ T cells, the supernatant from co-cultures of $CD4^+$ T cells and myeloid dendritic cells (mDCs) significantly upregulated the levels of IL-5, IL-13, and GATA3 in ILC2, both in terms of percentages and mRNA expression. Conversely, the supernatant from co-cultures of mDCs and $CD4^+$ T cells treated with P-D2-derived EVs conspicuously blocked this upregulation effect. Furthermore, treatment with IL-4 was found to reverse the inhibitory effect of P-D2-derived EVs (Fig. 8D, E). This suggests that P-D2-EVs may inhibit ILC2 activation through the mediation of DCs-mediated Th2 differentiation. Consistent results were obtained using ELISA to measure the levels of IL13 and IL5 in the conditioned medium (Fig. 8F).

In order to further validate the correlation between P-D2-EVs regulation of DCs in inhibiting Th2 differentiation and the inactivation of the Fut1/ICAM1/P38 MAPK signaling pathway, we examined the effect of co-culture supernatants of Fut1 overexpressing mDCs and $CD4^+$ T cells on ILC2 activation. Flow cytometry results showed that compared to the $ILC2^+CD4^+$ T + NC-OE-mDCs group, the co-culture supernatants of Fut1 overexpressing mDCs and $CD4^+$ T cells upregulated the percentage and mRNA expression of IL5, IL13 and GATA3 in ILC2, as well as the level of IL5, IL13 in the cell supernatant. However, this upregulation was significantly counteracted by co-incubation with IL4-neutralizing antibodies and also attenuated by pre-treatment of ILC2 cells with IL4Rα blocking antibodies (Fig. 8G–I). These results further confirm that P-D2-EVs inhibit DCs through the Fut1/ICAM1/P38 MAPK axis, thus reducing Th2 differentiation and ultimately inhibiting ILC2 activation.

Following this, we further investigated the inhibitory effect of P-D2-EVs on ILC2 activation in AR mice. We used flow cytometry to isolate ILC2 (CD45 + Lineage-KLRG1 + CD90.2 + Lymphocytes) from mouse nasal tissues (Fig. S9A). Flow cytometry analysis of ILC2 in nasal tissues of the Control group, Model group, and Model + P-D2-EVs group revealed that compared to the Model group, the Model + P-D2-EVs group exhibited a significant reduction in the proportion of ILC2 cells (Fig. S9B). Subsequent flow cytometry analysis found that compared to the Control group, the proportion of IL13 and GATA3 positive cells in ILC2 of the Model group significantly increased, but treatment with P-D2-EVs reversed this effect in the Model mice (Fig. S9C). RT-qPCR analysis of IL13 and GATA3 mRNA expression in ILC2 further confirmed the inhibitory effect of P-D2-EVs on ILC2 activation in the AR model mice (Fig. S9D). These results suggest that P-D2-EVs inhibit ILC2 activation in AR mice.

Based on the above results, it is evident that P-D2-EVs reshape DC metabolism to suppress Th2 differentiation by inhibiting the activation of the Fut1/ICAM1/P38 MAPK pathway, thereby inhibiting ILC2 activation in AR mice.

P-D2-EVs alleviate AR by modulating the Fut1/ICMA1/P38 mapk pathway

To investigate the regulatory mechanism of P-D2-EVs in treating AR in mice further, we established an AR mouse model by transferring DCs (Fig. S10). Compared to the Model + P-D2-EVs + NC-OE-mDCs group, the Model + P-D2-EVs + Fut1-OE-mDCs group exhibited a significant increase in the frequency of nose rubbing and sneezing in mice (Fig. 9A). Additionally, in the Model + P-D2-EVs + Fut1-OE-mDCs group, the overexpression of Fut1 in DCs restored the inhibitory effect of P-D2-EVs on total cell count in NALF, serum OVA-specific IgE levels, and goblet cell percentage (Fig. 9B–D). H&E staining results demonstrated that compared to the Model + P-D2-EVs + NC-OE-mDCs group, Fut1-OE-mDCs treatment in the Model + P-D2-EVs + Fut1-OE-mDCs group hindered the improvement of P-D2-EVs on the number of eosinophils in the OVA-induced nasal mucosa, nasal mucosal thickness, and neutrophil infiltration (Fig. 9E, F). These results indicate that Fut1 overexpression in DCs can counteract the therapeutic effect of P-D2-EVs on AR.

Moreover, we explored the expression of Fut1/ICMA1/P38 MAPK pathway-related factors in nasal tissue.

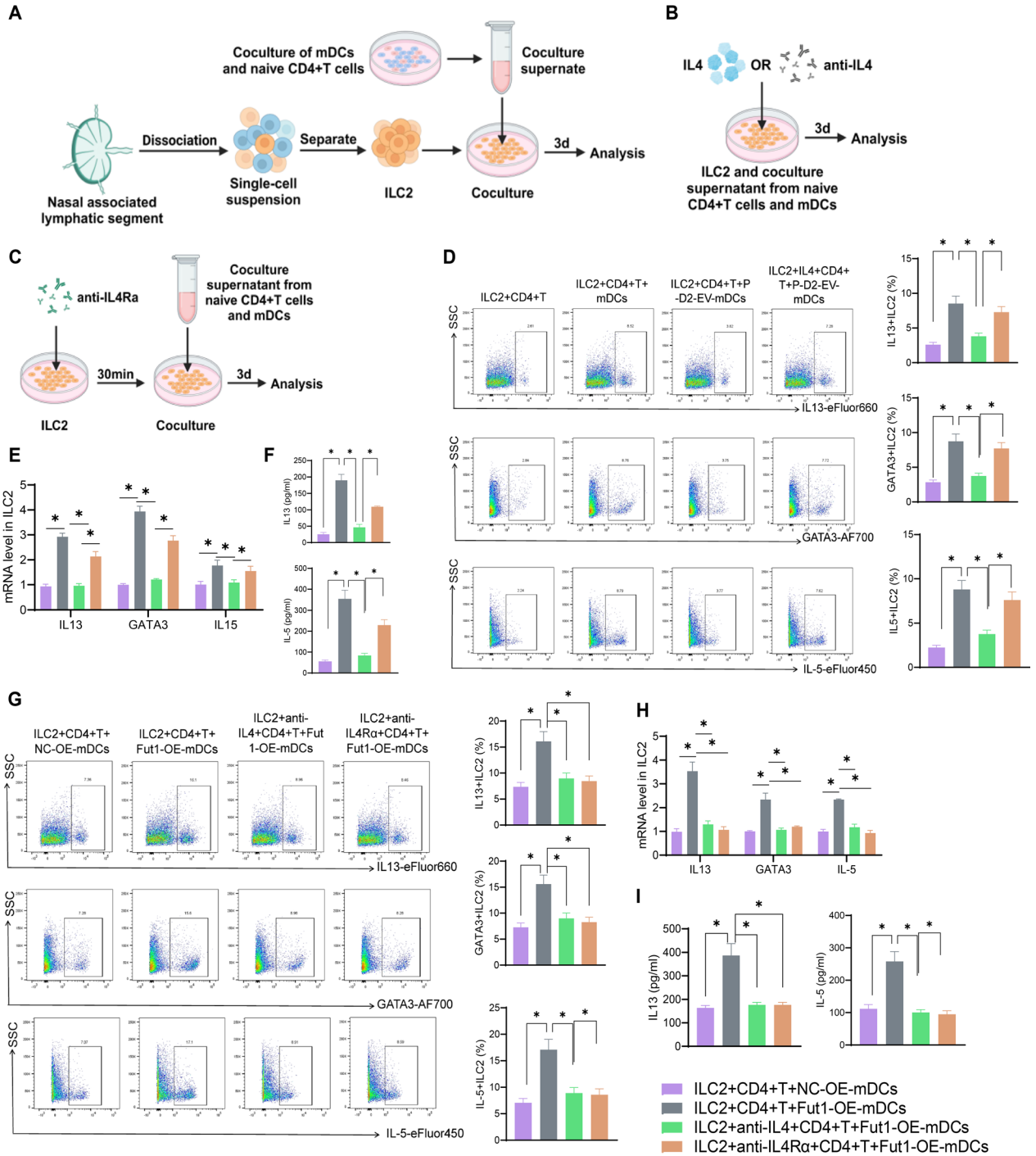

Fig. 8 Influence of P-D2-EVs-mediated DCs metabolic regulation on Th2 differentiation and activation of ILC2 cells. **A** Schematic diagram of ILC2 cell extraction and co-culture. **B**, **C** Schematic diagram of IL4, IL4 antibody, and IL4Rα antibody treatment. **D** Flow cytometry analysis of the percentage of IL5, IL13 and GATA3 in ILC2 cells treated with supernatant from co-culture of different treated mDCs and $CD4^+$ T cells. **E** RT-qPCR analysis of the effects of supernatant from co-culture of different treated mDCs and $CD4^+$ T cells on mRNA expression of IL5, IL13 and GATA3 in ILC2 cells. **F** ELISA analysis of the impact of supernatant from co-culture of different treated mDCs and $CD4^+$ T cells on the level of IL5, IL13 in the supernatant of ILC2 cells. **G** Flow cytometry analysis of the percentage of IL5, IL13 and GATA3 in ILC2 cells treated with supernatant from co-culture of different treated mDCs and $CD4^+$ T cells. **H** RT-qPCR analysis of the effects of supernatant from co-culture of different treated mDCs and $CD4^+$ T cells on mRNA expression of IL5, IL13 and GATA3 in ILC2 cells. **I** ELISA analysis of the impact of supernatant from co-culture of different treated mDCs and $CD4^+$ T cells on the level of IL5, IL13 in the supernatant of ILC2 cells; *denotes $P < 0.05$ when compared between two groups, all experiments were repeated three times

Compared to the Control group, the Model group significantly upregulated Fut1 expression, the ratio of p-P38/P38, and promoted ICAM1 fucosylation; however, P-D2-EVs treatment reversed this phenomenon (Fig. 9G–I). Subsequently, we measured the expression of DCs, Th2, ILC2-related genes and the levels of secreted markers in nasal tissue by RT-qPCR and ELISA. The results showed that compared to the Model group, P-D2-EVs treatment in the Model + P-D2-EVs group blocked the suppression of IL10 expression and secretion, promoted the expression and secretion of IL4 and IL13, and upregulated GATA3 expression in OVA-induced mice (Fig. 9J, K). This suggests that P-D2-EVs downregulate ILC2 activation by mediating metabolic inhibition of Th2 differentiation through the inactivation of the Fut1/ICMA1/P38 MAPK pathway in DCs.

To further investigate this regulatory mechanism, we utilized Western blot analysis to compare the expression levels of Fut1, the ratio of p-P38/P38, and the fucosylation of ICAM1 in DCs between the Model + P-D2-EVs + NC-OE-mDCs group and the Model + P-D2-EVs + Fut1-OE-mDCs group (Fig. 9L–N). Our results showed that overexpressing Fut1 in DCs significantly restored the expression of Fut1, the p-P38/P38 ratio, and the fucosylation of ICAM1, which were improved by P-D2-EVs. Furthermore, the intervention of Fut1 overexpressing mDCs counteracted the regulatory effects of P-D2-EVs on IL10, IL4, IL13, and GATA3 expression and secretion (Fig. 9O, P). Additional in vivo experiments confirmed the inhibitory effect of P-D2-EVs on the activation of the Fut1/ICAM1/P38 MAPK pathway.

Subsequently, we isolated DCs, Th2, and ILC2 cells from mouse nasal tissues and analyzed them through flow cytometry. Compared to the Model + NC-OE-mDCs group, treatment with P-D2-EVs in the Model + P-D2-EVs + NC-OE-mDCs group reduced the proportions of DCs, Th2, and ILC2 cells. Additionally, it increased the proportion of IL10-positive cells in DCs, decreased the proportion of GATA3-positive cells in Th2 cells, and downregulated the percentage of IL13 and GATA3-positive cells in ILC2 (Fig. 10A–G). Moreover, when Fut1 overexpressing mDCs were used to block the trend changes induced by P-D2-EVs treatment in the Model + P-D2-EVs + NC-OE-mDCs group, the results remained consistent. These findings further confirm that P-D2-EVs reshape DCs' IL10 metabolism, inhibit Th2 differentiation, and dampen ILC2 activation by suppressing the Fut1/ICAM1/P38 MAPK pathway.

Overall, our results demonstrate that the novel MSCs nanovesicles P-D2-EVs alleviate AR by inhibiting the activation of the Fut1/ICAM1/P38 MAPK pathway, restoring DCs' IL10 metabolism, inhibiting Th2 differentiation, and reducing ILC2 activation.

Discussion

AR is a common immune-mediated disease involving the activation and interaction of various immune cells [7, 8, 77]. Existing treatment methods for AR have limited control efficacy, highlighting the need for new therapeutic strategies. In recent years, MSC-derived nanovesicles, known as MSCs nanovesicles, have shown potential in the treatment of immune-mediated diseases [78–80]. This study aims to explore the interaction between P-D2-EVs nanovesicles and DCs, Th2, and ILC2 through single-cell and transcriptomic sequencing analysis. The goal is to uncover novel mechanisms of nanovesicle therapy for AR.

In this study, we prepared MSCs nanovesicles, specifically targeted to DCs, named P-D2-EVs. These nanovesicles were comprehensively characterized and subjected to in vivo and in vitro tracer analysis, confirming their effective targeting of DCs [81–84]. This

(See figure on next page.)

Fig. 9 In vivo validation of the regulatory mechanism of P-D2-EVs. **A** Number of nasal itching and sneezing events within 2 h after the final intranasal OVA administration in each group of mice (n = 6). **B** Total cell count in NALF of each group of mice (n = 6). **C** OVA-specific serum IgE levels in each group of mice (n = 6). **D** Representative PAS staining images (scale bar = 100 μm) and quantification of PAS-positive goblet cells in nasal tissue of each group of mice (n = 6). **E** Representative H&E staining images (scale bar = 100 μm or 25 μm) of nasal tissue, as well as quantification of eosinophils and nasal mucosal thickness, with the red arrow indicating nasal mucosa (n = 6). **F** Representative images (scale bar = 25 μm) and quantification of neutrophil infiltration in nasal mucosa of each group of mice, with the black arrow indicating positive cells (n = 6). **G** Protein expression and quantification of Fut1, p-P38, and P3J8 in nasal tissue of each group of mice as detected by Western blotting (n = 6). **H** α-(1,2)-Fucose glycosylation status and quantification of ICAM1 protein in nasal tissue of each group of mice as detected by Western blotting following UEA-1 enrichment (n = 6). **I** Binding and quantification of ICAM1 and UEA1 in nasal tissue of each group of mice as detected by co-immunoprecipitation (n = 6). **J** Expression and quantification of IL10, IL4, IL13, and GATA3 in nasal tissue of each group of mice as detected by RT-qPCR (n = 6). **K** Levels of IL10, IL4, and IL13 in serum of each group of mice as detected by ELISA (n = 6). **L** Protein expression and quantification of Fut1, p-P38, and P3J8 in nasal tissue of each group of mice as detected by Western blotting (n = 6). **M** α-(1,2)-Fucose glycosylation status and quantification of ICAM1 protein in nasal tissue of each group of mice as detected by Western blotting following UEA-1 enrichment (n = 6). **N** Binding and quantification of ICAM1 and UEA1 in nasal tissue of each group of mice as detected by co-immunoprecipitation (n = 6). **O** Expression and quantification of IL10, IL4, IL13, and GATA3 in nasal tissue of each group of mice as detected by RT-qPCR (n = 6). **P** Levels of IL10, IL4, and IL13 in serum of each group of mice as detected by ELISA (n = 6); *NALF* nasal lavage fluid; *indicates significant difference between two groups with $P < 0.05$

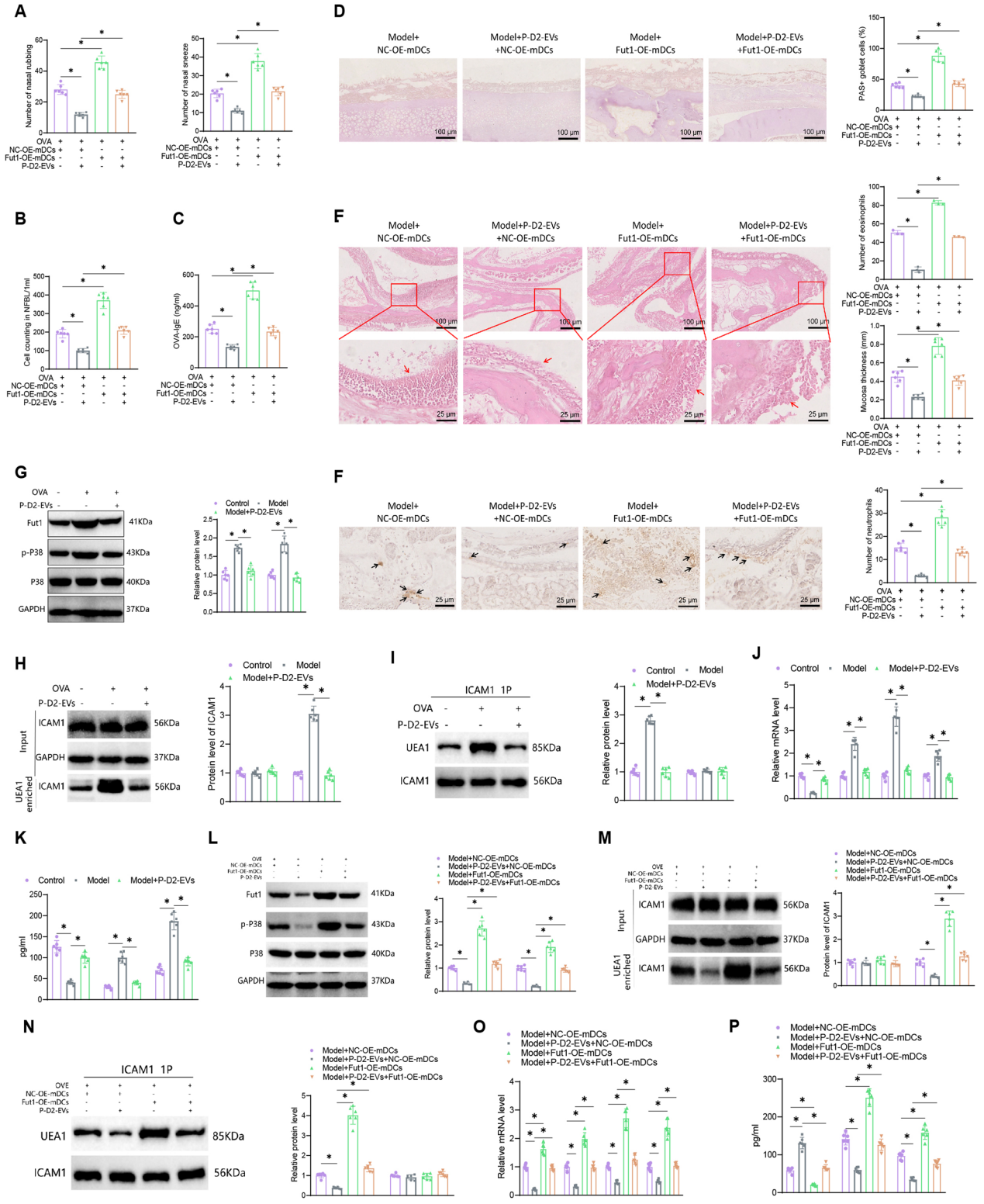

Fig. 9 (See legend on previous page.)

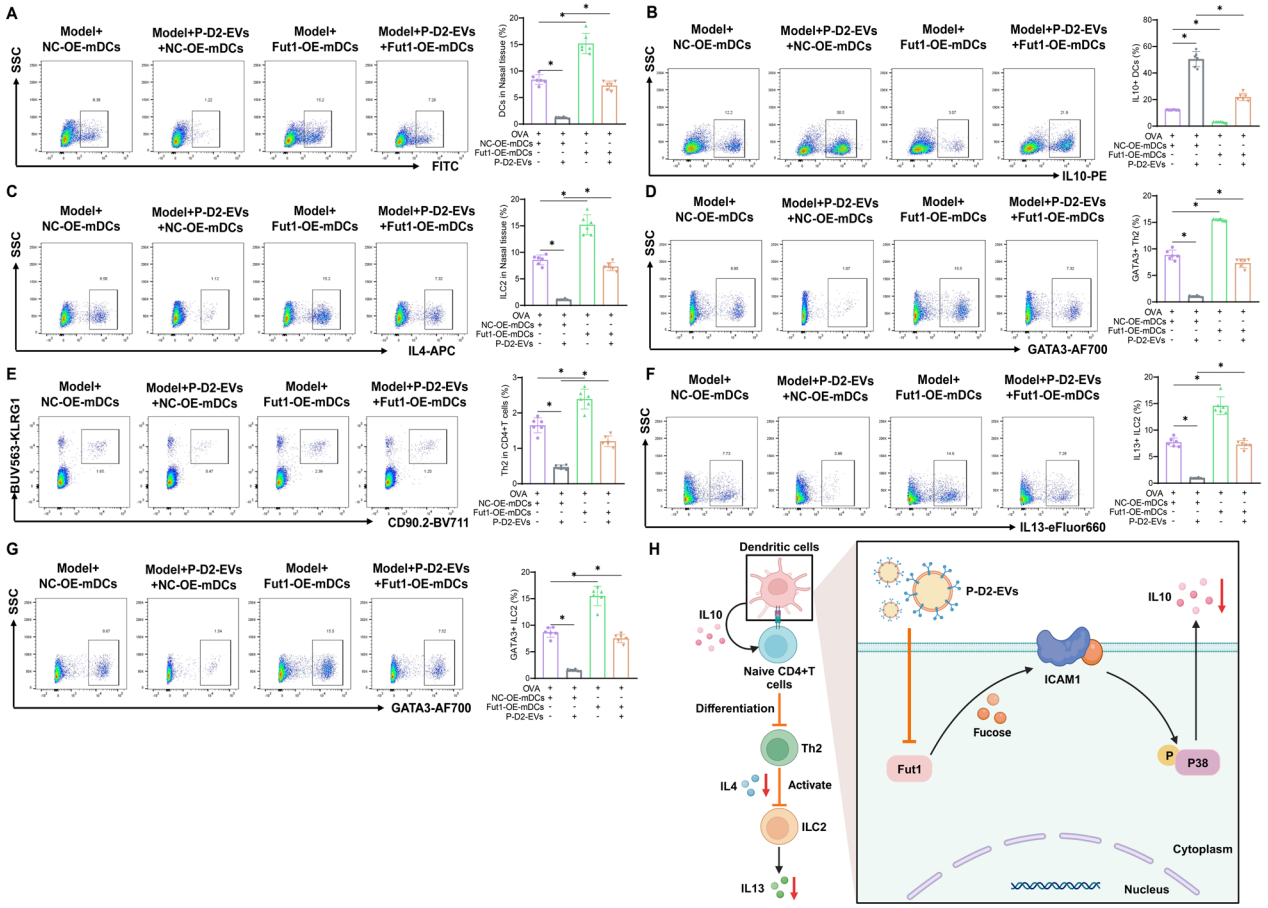

Fig. 10 Mechanism of P-D2-EVs regulation of DCs metabolism, Th2 differentiation, and ILC2 activation in vivo. **A** Percentage of DCs in nasal tissue of each group of mice as analyzed by flow cytometry (n = 6). **B** Percentage of IL10-positive DCs in nasal tissue of each group of mice as analyzed by flow cytometry (n = 6). **C** Percentage of Th2 cells among $CD4^+$ T cells in nasal tissue of each group of mice as analyzed by flow cytometry (n = 6). **D** Percentage of GATA3-positive cells among Th2 cells in nasal tissue of each group of mice as analyzed by flow cytometry (n = 6). **E** Percentage of ILC2 cells in nasal tissue of each group of mice as analyzed by flow cytometry (n = 6). **F** Percentage of IL13-positive cells among ILC2 cells in nasal tissue of each group of mice as analyzed by flow cytometry (n = 6). **G** Percentage of GATA3-positive cells among ILC2 cells in nasal tissue of each group of mice as analyzed by flow cytometry (n = 6); *indicates significant difference between two groups with $P < 0.05$. **H** Illustration of the molecular mechanism underlying the improvement of AR by P-D2-EVs

characteristic provides a solid foundation for the application of nanovesicles in AR treatment and suggests that P-D2-EVs may serve as an innovative therapeutic strategy [85, 86]. In our in vitro experiments, we discovered that P-D2-EVs can inhibit IL10 metabolism in DCs, thereby suppressing Th2 differentiation and further inhibiting the activation of ILC2 cells. These results support the potential of P-D2-EVs in regulating immune cell activation and interaction.

Compared to previous studies, this research has made breakthroughs in nanovesicle preparation and the understanding of AR treatment mechanisms. Firstly, we successfully prepared MSCs nanovesicles named P-D2-EVs that specifically target DCs, providing advantages for AR treatment [87–89]. Due to the specific immunomodulatory properties of P-D2-EVs, they may exhibit superior targeting efficacy over conventional medications, potentially reducing unnecessary systemic side effects [90]. If P-D2-EVs demonstrate prolonged therapeutic effects in clinical settings, it could decrease patients' dependence on daily antihistamines and corticosteroids [91]. Moreover, as P-D2-EVs can directly interact with target cells, they may provide faster clinical improvement compared to traditional drug therapies. Secondly, by employing combined transcriptomic and single-cell sequencing analyses, we delved into the mechanisms by which P-D2-EVs regulate DCs, Th2, and ILC2 cells [92–94]. This integrative analytical approach yields more comprehensive insights, facilitating a thorough understanding of the nanovesicles' role in AR therapy.

By bioinformatics analysis, we identified the core gene Fut1, which is associated with the intersection of differentially expressed genes in the transcriptome. Further experimental verification demonstrated that P-D2-EVs downregulated Fut1 expression to inhibit fucosylation modification of DCs, suppressing the activation of the P38 MAPK signaling pathway, improving IL10 metabolism in DCs, and consequently inhibiting Th2 differentiation and ILC2 activation [95, 96]. This discovery reveals important mechanisms by which P-D2-EVs regulate DC metabolism and immune cell interaction.

By establishing an AR mouse model and treating it with P-D2-EVs, we observed that P-D2-EVs could reshape DC metabolism, suppress Th2 differentiation, and further inhibit ILC2 activation by inhibiting the Fut1/ICAM1/P38 MAPK signaling pathway. These results not only verified the therapeutic effect of P-D2-EVs in vivo but also provided potential mechanisms for nanovesicle therapy in AR, thus offering important insights for the clinical application of this treatment strategy [97, 98].

In conclusion, we can preliminarily conclude that the novel MSCs nanovesicles P-D2-EVs inhibit ICAM1 fucosylation modification by downregulating Fut1 expression, suppress the activation of the P38 MAPK pathway, restore DCs' IL10 metabolism, and inhibit Th2 differentiation, ultimately reducing ILC2 activation and alleviating AR (Fig. 10H).

The findings of this study have important scientific and clinical value, providing significant references for the development of novel AR treatment strategies. However, this study also has limitations, such as the focus on mouse models and the need for further verification of the effects in humans. Insufficient safety data currently exist regarding the long-term use of P-D2-EVs. Therefore, we recommend conducting extended animal studies as well as preliminary human safety research. The optimal dosage of P-D2-EVs has yet to be precisely determined, necessitating a multi-phase dose escalation study. Moreover, potential unknown side effects of P-D2-EVs should be monitored and assessed through comprehensive preclinical and clinical trials, particularly focusing on potential long-term impacts on the immune system. Furthermore, the study of related regulatory mechanisms and signaling pathways still requires further exploration, and future research can investigate the molecular interactions between P-D2-EVs and immune cells, as well as optimize the preparation and delivery systems of nanovesicles.

Although this study has made important discoveries, there are still some issues that need to be addressed. For example, the preparation and delivery system of nanovesicles needs to be further optimized to improve its targeting specificity and therapeutic effectiveness. Additionally, the interaction of nanovesicles with other immune cell types needs to be studied to gain a more comprehensive understanding of their therapeutic effects. Future research can also explore the potential application of nanovesicles in other immune-related diseases and further optimize treatment plans to achieve better clinical translation.

Supplementary Information

The online version contains supplementary material available at https://doi.org/10.1186/s12951-024-02748-2.

Supplementary Material 1: Fig. S1. Preparation, characterization and uptake of EVs and P-D2-EVs. Note:Flowchart of P-D2-EVs preparation;Western blot detection of EVs and P-D2-EVs;TEM representative images of EVs and P-D2-EVs;NTA measurement of average particle size of EVs and P-D2-EVs;NTA measurement of Zeta potential of EVs and P-D2-EVs;Concentration changes of EVs and P-D2-EVs in PBS for 30 days;Particle size changes of EVs and P-D2-EVs in PBS for 30 days;Quantification of P-D2 peptide decorated on EVs by CBQCA assay. Red dots indicate the initial amount of P-D2 peptide added, while black dots show the amount of P-D2 peptide conjugated on EVs after purification by size exclusion chromatography. The left graph shows the standard curve for measuring P-D2 peptide by CBQCA assay.Representative imagesand fluorescence intensity quantification of DCs uptake of EVs and P-D2-EVs, where blue represents cell nucleus, red represents cell membrane, green represents EVs or P-D2-EVs, and white arrows indicate EVs or P-D2-EVs uptake by DCs; MSCs: Mesenchymal stem cells, EVs: Extracellular vesicles, n.s.: not significant, * represents statistical significance, all experiments were repeated three times.

Supplementary Material 2: Fig. S2. Targeting of EVs and P-D2-EVs to DCs in vivo. Note:Schematic diagram of the detection of *in vivo* targeting of EVs and P-D2-EVs to DCs using live fluorescence imaging and flow cytometry;Representative images of live fluorescence imaging and quantitative analysis of fluorescence intensity of EVs and P-D2-EVs in the nasal tissue of AR model mice at 6h and 12h post-administration, with color intensity ranging from weak to strong;Flow cytometric analysis of EVs and P-D2-EVs targeting DCs in the nasal tissue of AR model miceand quantitative analysis of fluorescence intensity of DiR in DCs; OV: ovalbumin, DCs: Dendritic cells; * indicates statistically significant difference compared to the control group at $p < 0.05$.

Supplementary Material 3: Fig. S3. Quality control, filtering, and principal component analysis of scRNA-seq data. Note:Violin plots showing the number of genes, number of mRNA molecules, and percentage of mitochondrial genesin each cell of the nasal tissue scRNA-seq data of Model groupand Model+P-D2-EVs group;Scatter plots showing the correlation between filtered data nCount_RNA and percent.mt, and between nCount_RNA and nFeature_RNA;Identification of highly variable genes in the samples through variance analysis;Cell cycle status of each cell in the scRNA-seq data, with S.Score representing S phase and G2M.Score representing G2M phase;Distribution of standard deviation of PCs, with important PCs having larger standard deviations;p-values of the top 50 PCs obtained from PCA analysis;Feature genes in the top 2 PCs of PCA analysis;Heatmap showing the expression of the top 15 significantly correlated genes in PC_1 - PC_6 of PCA, with yellow indicating upregulation and purple indicating downregulation;Distribution of cells in PC_1 and PC_2 before batch correction, with each dot representing a cell and different colors representing different samples.

Supplementary Material 4: Fig. S4. UMAP clustering tree of scRNA-seq data. Note: Branches represent the clustering relationship of cells, while dots represent cell clusters, with the size of dots typically indicating cell abundance.

Supplementary Material 5: Fig. S5. Expression of marker genes for DCs, T cells, and ILC2. Note: Expression of marker genes for DCs, T cells, and ILC2 in different subpopulations of nasal tissue samples from the Model

groupand Model+P-D2-EVs groupmice, with darker purple indicating higher average expression levels.

Supplementary Material 6: Fig. S6. Key genes regulated by P-D2-EVs in DCs were identified using bioinformatics analysis. Note:Volcano plot of differentially expressed genesin DCs obtained from nasal tissue samples of the Model groupand Model+P-D2-EVs groupas determined by single-cell sequencing. The red dots to the left of the dotted line represent genes highly expressed in DCs, while the red dots to the right represent genes with low expression in DCs;Venn diagram showing the intersection between ScRNA-DEGs and DEGs obtained from transcriptome sequencing;Venn diagram showing genes highly expressed in both sequencing results;Venn diagram showing genes with low expression in both sequencing results;Differential expression of B-DEGs observed in transcriptome sequencing;Differential expression of B-DEGs observed in single-cell sequencing;GO enrichment analysis results of B-DEGs;KEGG enrichment analysis results of B-DEGs.

Supplementary Material 7: Fig. S7. Effects of P-D2-EVs on the differentiation and maturation phenotype of DCs. Note:Schematic diagram of iDCs and iDCs+P-D2-EVs generation;Flow cytometric analysis of surface marker expression on iDCs in different treatment groups and quantitative analysis of average fluorescence intensity;Schematic diagram of mDCs and mDCs+P-D2-EVs generation;Flow cytometric analysis of surface marker expression on mDCs in different treatment groups and quantitative analysis of average fluorescence intensity; * indicates statistically significant difference compared to the control group at $p<0.05$, all experiments were repeated 3 times.`

Supplementary Material 8: Fig. S8. *In vivo* validation of the effects of P-D2-EVs on Th2 differentiation. Note:Strategy for the isolation of Th2 cells by flow cytometry in nasal tissue of mice;Flow cytometric analysis of the percentage of Th2 cells in $CD4^+$ T cells in nasal tissue of different groups of mice;Flow cytometric analysis of the percentage of GATA3-positive cells in Th2 cells in nasal tissue of different groups of mice;RT-qPCR analysis of mRNA expression of IL4 and GATA3 in Th2 cells in nasal tissue of different groups of mice; * indicates statistically significant difference compared to the control group at $P< 0.05$.

Supplementary Material 9: Fig. S9. In vivo validation of the influence of P-D2-EVs on ILC2 activation. Note:Flow cytometry isolation strategy of ILC2 cells in mouse nasal tissue;Flow cytometry analysis of the percentage of ILC2 cells in nasal tissues of different groups of mice;Flow cytometry analysis of the percentage of IL13 and GATA3 positive cells in ILC2 cells in nasal tissues of different groups of mice;RT-qPCR analysis of mRNA expression of IL13 and GATA3 in ILC2 cells in nasal tissues of different groups of mice; * $P < 0.05$ when compared between two groups..

Supplementary Material 10: Fig. S10. Construction of the mDCs adoptive transfer AR mouse model.

Supplementary Material 11.

Acknowledgements
None.

Author contributions
Jianyu Liu: Conceptualization, experimental design, manuscript drafting. Meiqun Wang: In vitro experiments, data analysis, manuscript revision. Xiaoyan Tian: Transcriptomic sequencing, data analysis. Shuhong Wu: Animal experiments, validation of results. Haisen Peng: Single-cell sequencing, data interpretation. Yaqiong Zhu: Fabrication and characterization of nanovesicles. Yuehui Liu: Supervision, resources, manuscript review.

Funding
Not applicable.

Data availability
All data can be provided as needed.

Declarations

Ethics approval and consent to participate
All animal experiments were approved by the Animal Ethics Committee of Jiangxi Medical College, Nanchang University (NCULAE-20221031024).

Competing interests
The author declares no competing interests.

Received: 30 January 2024 Accepted: 2 August 2024
Published online: 19 September 2024

References

1. Drazdauskaitė G, Layhadi JA, Shamji MH. Mechanisms of allergen immunotherapy in allergic rhinitis. Curr Allergy Asthma Rep. 2020;21(1):2. https://doi.org/10.1007/s11882-020-00977-7.
2. Bai X, Liu P, Shen H, Zhang Q, Zhang T, Jin X. Water-extracted *Lonicera japonica* polysaccharide attenuates allergic rhinitis by regulating NLRP3-IL-17 signaling axis. Carbohydr Polym. 2022;297: 120053. https://doi.org/10.1016/j.carbpol.2022.120053.
3. Dwyer DF, Ordovas-Montanes J, Allon SJ, et al. Human airway mast cells proliferate and acquire distinct inflammation-driven phenotypes during type 2 inflammation. Sci Immunol. 2021;6(56): eabb7221. https://doi.org/10.1126/sciimmunol.abb7221.
4. Liu F, Chen N, Wang R, Zhang L, Li Y. Visual analysis of allergic rhinitis in children based on web of science and CiteSpace software. Front Pediatr. 2022;10: 911293. https://doi.org/10.3389/fped.2022.911293.
5. Yao X, Liu Y, Jiao H, Ma W, Chen M. Association of LOX gene G473A polymorphism with the occurrence of allergic rhinitis and efficacy of montelukast sodium in children. Cell Cycle. 2023;22(20):2280–7. https://doi.org/10.1080/15384101.2023.2286802.
6. Wise SK, Damask C, Roland LT, et al. International consensus statement on allergy and rhinology: allergic rhinitis—2023. Int Forum Allergy Rhinol. 2023;13(4):293–859. https://doi.org/10.1002/alr.23090.
7. Zhang Y, Lan F, Zhang L. Advances and highlights in allergic rhinitis. Allergy. 2021;76(11):3383–9. https://doi.org/10.1111/all.15044.
8. Bousquet J, Anto JM, Bachert C, et al. Allergic rhinitis. Nat Rev Dis Primers. 2020;6(1):95. https://doi.org/10.1038/s41572-020-00227-0.
9. Lan T, Luo M, Wei X. Mesenchymal stem/stromal cells in cancer therapy. J Hematol Oncol. 2021;14(1):195. https://doi.org/10.1186/s13045-021-01208-w.
10. Hoang DM, Pham PT, Bach TQ, et al. Stem cell-based therapy for human diseases. Signal Transduct Target Ther. 2022;7(1):272. https://doi.org/10.1038/s41392-022-01134-4.
11. Jo H, Brito S, Kwak BM, Park S, Lee MG, Bin BH. Applications of mesenchymal stem cells in skin regeneration and rejuvenation. Int J Mol Sci. 2021;22(5):2410. https://doi.org/10.3390/ijms22052410.
12. Zhang Z, Shang J, Yang Q, et al. Exosomes derived from human adipose mesenchymal stem cells ameliorate hepatic fibrosis by inhibiting PI3K/Akt/mTOR pathway and remodeling choline metabolism. J Nanobiotechnol. 2023;21(1):29. https://doi.org/10.1186/s12951-023-01788-4.
13. Yuan YG, Wang JL, Zhang YX, Li L, Reza AMMT, Gurunathan S. Biogenesis, composition and potential therapeutic applications of mesenchymal stem cells derived exosomes in various diseases. Int J Nanomed. 2023;18:3177–210. https://doi.org/10.2147/IJN.S407029.
14. Kodam SP, Ullah M. Diagnostic and therapeutic potential of extracellular vesicles. Technol Cancer Res Treat. 2021;20:15330338211041204. https://doi.org/10.1177/15330338211041203.
15. Kocholata M, Prusova M, Auer Malinska H, Maly J, Janouskova O. Comparison of two isolation methods of tobacco-derived extracellular vesicles, their characterization and uptake by plant and rat cells. Sci Rep. 2022;12(1):19896. https://doi.org/10.1038/s41598-022-23961-9.
16. Jovic D, Liang X, Zeng H, Lin L, Xu F, Luo Y. Single-cell RNA sequencing technologies and applications: a brief overview. Clin Transl Med. 2022;12(3): e694. https://doi.org/10.1002/ctm2.694.

17. Lei Y, Tang R, Xu J, et al. Applications of single-cell sequencing in cancer research: progress and perspectives. J Hematol Oncol. 2021;14(1):91. https://doi.org/10.1186/s13045-021-01105-2.
18. Saeidian AH, Youssefian L, Vahidnezhad H, Uitto J. Research techniques made simple: whole-transcriptome sequencing by RNA-Seq for diagnosis of monogenic disorders. J Invest Dermatol. 2020;140(6):1117-1126.e1. https://doi.org/10.1016/j.jid.2020.02.032.
19. Haas C, Neubauer J, Salzmann AP, Hanson E, Ballantyne J. Forensic transcriptome analysis using massively parallel sequencing. Forensic Sci Int Genet. 2021;52: 102486. https://doi.org/10.1016/j.fsigen.2021.102486.
20. Liu Y, Xia P, Yan F, et al. Engineered extracellular vesicles for delivery of an IL-1 receptor antagonist promote targeted repair of retinal degeneration. Small. 2023;19(46): e2302962. https://doi.org/10.1002/smll.202302962.
21. Lewis JS, Zaveri TD, Crooks CP 2nd, Keselowsky BG. Microparticle surface modifications targeting dendritic cells for non-activating applications. Biomaterials. 2012;33(29):7221–32. https://doi.org/10.1016/j.biomaterials.2012.06.049.
22. Yi S, Zhang X, Sangji H, et al. Surface engineered polymersomes for enhanced modulation of dendritic cells during cardiovascular immunotherapy. Adv Funct Mater. 2019;29(42):1904399. https://doi.org/10.1002/adfm.201904399.
23. Li Y, Zhang J, Shi J, et al. Exosomes derived from human adipose mesenchymal stem cells attenuate hypertrophic scar fibrosis by miR-192–5p/IL-17RA/Smad axis [published correction appears in Stem Cell Res Ther. 2021 Sep 3;12(1):490. 10.1186/s13287-021-02568-3]. Stem Cell Res Ther. 2021;12(1):221. https://doi.org/10.1186/s13287-021-02290-0.
24. He L, Zhu C, Jia J, et al. ADSC-Exos containing MALAT1 promotes wound healing by targeting miR-124 through activating Wnt/β-catenin pathway. Biosci Rep. 2020;40(5):BSR20192549. https://doi.org/10.1042/BSR20192549.
25. Gangadaran P, Rajendran RL, Lee HW, et al. Extracellular vesicles from mesenchymal stem cells activates VEGF receptors and accelerates recovery of hindlimb ischemia. J Control Release. 2017;264:112–26. https://doi.org/10.1016/j.jconrel.2017.08.022.
26. Zhou X, Chu X, Yuan H, et al. Mesenchymal stem cell derived EVs mediate neuroprotection after spinal cord injury in rats via the microRNA-21-5p/FasL gene axis. Biomed Pharmacother. 2019;115: 108818. https://doi.org/10.1016/j.biopha.2019.108818.
27. Mo LH, Han HY, Jin QR, et al. T cell activator-carrying extracellular vesicles induce antigen-specific regulatory T cells. Clin Exp Immunol. 2021;206(2):129–40. https://doi.org/10.1111/cei.13655.
28. Stark JM, Coquet JM, Tibbitt CA. The role of PPAR-γ in allergic disease. Curr Allergy Asthma Rep. 2021;21(11):45. https://doi.org/10.1007/s11882-021-01022-x.
29. McCusker CT. Use of mouse models of allergic rhinitis to study the upper and lower airway link. Curr Opin Allergy Clin Immunol. 2004;4(1):11–6. https://doi.org/10.1097/00130832-200402000-00004.
30. Ji KY, Jung DH, Pyun BJ, et al. Angelica gigas extract ameliorates allergic rhinitis in an ovalbumin-induced mouse model by inhibiting Th2 cell activation. Phytomedicine. 2021;93: 153789. https://doi.org/10.1016/j.phymed.2021.153789.
31. Cho SW, Zhang YL, Ko YK, et al. Intranasal treatment with 1,25-dihydroxyvitamin D3 alleviates allergic rhinitis symptoms in a mouse model. Allergy Asthma Immunol Res. 2019;11(2):267–79. https://doi.org/10.4168/aair.2019.11.2.267.
32. Wang M, Li Y, Yang J, Wang X, Zhang L. Genes related to allergen exposure in allergic rhinitis: a gene-chip-based study in a mouse model. BMC Med Genomics. 2022;15(1):243. https://doi.org/10.1186/s12920-022-01389-4.
33. Kim B, Lee YE, Yeon JW, et al. A novel therapeutic modality using CRISPR-engineered dendritic cells to treat allergies. Biomaterials. 2021;273: 120798. https://doi.org/10.1016/j.biomaterials.2021.120798.
34. Zhao F, Wang M, Li S, et al. DACH1 inhibits SNAI1-mediated epithelial–mesenchymal transition and represses breast carcinoma metastasis. Oncogenesis. 2015;4(3): e143. https://doi.org/10.1038/oncsis.2015.3.
35. Liu XQ, Peng YQ, Huang LX, et al. Dendritic cells mediated by small extracellular vesicles derived from MSCs attenuated the ILC2 activity via PGE2 in patients with allergic rhinitis. Stem Cell Res Ther. 2023;14(1):180. https://doi.org/10.1186/s13287-023-03408-2.
36. Wu J, Huang QM, Liu Y, et al. Long-term hypoxic hUCMSCs-derived extracellular vesicles alleviates allergic rhinitis through triggering immunotolerance of their VEGF-mediated inhibition of dendritic cells maturation. Int Immunopharmacol. 2023;124(Pt B): 110875. https://doi.org/10.1016/j.intimp.2023.110875.
37. Qiu S, Luo X, Mo L, et al. TAFA4-IL-10 axis potentiate immunotherapy for airway allergy by induction of specific regulatory T cells. NPJ Vac. 2022;7(1):133. https://doi.org/10.1038/s41541-022-00559-w.
38. Peng YQ, Wu ZC, Xu ZB, et al. Mesenchymal stromal cells-derived small extracellular vesicles modulate DC function to suppress Th2 responses via IL-10 in patients with allergic rhinitis. Eur J Immunol. 2022;52(7):1129–40. https://doi.org/10.1002/eji.202149497.
39. Zhang L, Meng W, Chen X, Ning Y, Sun M, Wang R. MiR-150-5p regulates the functions of type 2 innate lymphoid cells via the ICAM-1/p38 MAPK axis in allergic rhinitis. Mol Cell Biochem. 2022;477(4):1009–22. https://doi.org/10.1007/s11010-021-04346-4.
40. Yu L, Sui B, Fan W, et al. Exosomes derived from osteogenic tumor activate osteoclast differentiation and concurrently inhibit osteogenesis by transferring COL1A1-targeting miRNA-92a-1-5p. J Extracell Vesicles. 2021;10(3): e12056. https://doi.org/10.1002/jev2.12056.
41. Qiao YL, Zhu MW, Xu S, et al. Allergen-induced CD11c + dendritic cell pyroptosis aggravates allergic rhinitis. Cell Commun Signal. 2023;21(1):281. https://doi.org/10.1186/s12964-023-01309-8.
42. Teng ZX, Zhou XC, Xu RT, et al. Tfh exosomes derived from allergic rhinitis promote DC maturation through miR-142-5p/CDK5/STAT3 pathway. J Inflamm Res. 2022;15:3187–205. https://doi.org/10.2147/JIR.S365217.
43. Deng YJ, Ren EH, Yuan WH, Zhang GZ, Wu ZL, Xie QQ. GRB10 and E2F3 as diagnostic markers of osteoarthritis and their correlation with immune infiltration. Diagnostics (Basel). 2020;10(3):171. https://doi.org/10.3390/diagnostics10030171.
44. Peng XY, Wang Y, Hu H, Zhang XJ, Li Q. Identification of the molecular subgroups in coronary artery disease by gene expression profiles. J Cell Physiol. 2019;234(9):16540–8. https://doi.org/10.1002/jcp.28324.
45. Golebski K, Layhadi JA, Sahiner U, et al. Induction of IL-10-producing type 2 innate lymphoid cells by allergen immunotherapy is associated with clinical response. Immunity. 2021;54(2):291-307.e7. https://doi.org/10.1016/j.immuni.2020.12.013.
46. Iinuma T, Kiuchi M, Hirahara K, et al. Single-cell immunoprofiling after immunotherapy for allergic rhinitis reveals functional suppression of pathogenic T^H2 cells and clonal conversion. J Allergy Clin Immunol. 2022;150(4):850-860.e5. https://doi.org/10.1016/j.jaci.2022.06.024.
47. Tian X, Liu B, Chen L, et al. RNA-Seq identifies marked Th17 cell activation and altered CFTR expression in different atopic dermatitis subtypes in chinese han populations. Front Immunol. 2021;12: 628512. https://doi.org/10.3389/fimmu.2021.628512.
48. Zhuo Z, Lin H, Liang J, et al. Mitophagy-related gene signature for prediction prognosis, immune scenery, mutation, and chemotherapy response in pancreatic cancer. Front Cell Dev Biol. 2022;9: 802528. https://doi.org/10.3389/fcell.2021.802528.
49. Shi Z, Jiang W, Wang M, et al. Inhibition of JAK/STAT pathway restrains TSLP-activated dendritic cells mediated inflammatory T helper type 2 cell response in allergic rhinitis. Mol Cell Biochem. 2017;430(1–2):161–9. https://doi.org/10.1007/s11010-017-2963-7.
50. Suzuki M, Yokota M, Ozaki S, Nakamura Y. A novel allergen-specific therapy with regulatory T cells induced by CD40-silenced dendritic cells. Asian Pac J Allergy Immunol. 2019;37(4):240–8. https://doi.org/10.12932/AP-240418-0302.
51. Gao WX, Sun YQ, Shi J, et al. Effects of mesenchymal stem cells from human induced pluripotent stem cells on differentiation, maturation, and function of dendritic cells. Stem Cell Res Ther. 2017;8(1):48. https://doi.org/10.1186/s13287-017-0499-0.
52. Loong JH, Wong TL, Tong M, et al. Glucose deprivation-induced aberrant FUT1-mediated fucosylation drives cancer stemness in hepatocellular carcinoma. J Clin Invest. 2021;131(11): e143377. https://doi.org/10.1172/JCI143377.
53. Yao Y, Cui L, Ye J, et al. Dioscin facilitates ROS-induced apoptosis via the p38-MAPK/HSP27-mediated pathways in lung squamous cell carcinoma. Int J Biol Sci. 2020;16(15):2883–94. https://doi.org/10.7150/ijbs.45710.
54. Lee CC, Lin CL, Leu SJ, Lee YL. Overexpression of Notch ligand Delta-like-1 by dendritic cells enhances their immunoregulatory capacity and exerts antiallergic effects on Th2-mediated allergic asthma in mice. Clin Immunol. 2018;187:58–67. https://doi.org/10.1016/j.clim.2017.10.005.
55. Lin CL, Huang HM, Hsieh CL, Fan CK, Lee YL. Jagged1-expressing adenovirus-infected dendritic cells induce expansion of $Foxp3^+$ regulatory T cells

and alleviate T helper type 2-mediated allergic asthma in mice. Immunology. 2019;156(2):199–212. https://doi.org/10.1111/imm.13021.
56. Lee YJ, Yassa C, Park SH, et al. Interactions between Malassezia and new therapeutic agents in atopic dermatitis affecting skin barrier and inflammation in recombinant human epidermis model. Int J Mol Sci. 2023;24(7):6171. https://doi.org/10.3390/ijms24076171.
57. Jha A, Ahad A, Mishra GP, et al. SMRT and NCoR1 fine-tune inflammatory versus tolerogenic balance in dendritic cells by differentially regulating STAT3 signaling. Front Immunol. 2022;13: 910705. https://doi.org/10.3389/fimmu.2022.910705.
58. He L, Guo Z, Wang W, Tian S, Lin R. FUT2 inhibits the EMT and metastasis of colorectal cancer by increasing LRP1 fucosylation. Cell Commun Signal. 2023;21(1):63. https://doi.org/10.1186/s12964-023-01060-0.
59. He C, Li A, Lai Q, et al. The DDX39B/FUT3/TGFβR-I axis promotes tumor metastasis and EMT in colorectal cancer. Cell Death Dis. 2021;12(1):74. https://doi.org/10.1038/s41419-020-03360-6.
60. Wang Z, Tan C, Duan C, et al. FUT2-dependent fucosylation of HYOU1 protects intestinal stem cells against inflammatory injury by regulating unfolded protein response. Redox Biol. 2023;60: 102618. https://doi.org/10.1016/j.redox.2023.102618.
61. Qu Y, Sun Z, Yuan Y, et al. Monocytic myeloid-derived suppressive cells mitigate over-adipogenesis of bone marrow microenvironment in aplastic anemia by inhibiting $CD8^+$ T cells. Cell Death Dis. 2022;13(7):620. https://doi.org/10.1038/s41419-022-05080-5.
62. Alam A, Levanduski E, Denz P, et al. Fungal mycobiome drives IL-33 secretion and type 2 immunity in pancreatic cancer. Cancer Cell. 2022;40(2):153-167.e11. https://doi.org/10.1016/j.ccell.2022.01.003.
63. Moffat JM, Segura E, Khoury G, et al. Targeting antigen to bone marrow stromal cell-2 expressed by conventional and plasmacytoid dendritic cells elicits efficient antigen presentation. Eur J Immunol. 2013;43(3):595–605. https://doi.org/10.1002/eji.201242799.
64. Upham JW, Stumbles PA. Why are dendritic cells important in allergic diseases of the respiratory tract? Pharmacol Ther. 2003;100(1):75–87. https://doi.org/10.1016/s0163-7258(03)00094-9.
65. McKenzie AN. Type-2 innate lymphoid cells in asthma and allergy. Ann Am Thorac Soc. 2014;11(Suppl 5):S263–70. https://doi.org/10.1513/AnnalsATS.201403-097AW.
66. Symowski C, Voehringer D. Th2 cell-derived IL-4/IL-13 promote ILC2 accumulation in the lung by ILC2-intrinsic STAT6 signaling in mice. Eur J Immunol. 2019;49(9):1421–32. https://doi.org/10.1002/eji.201948161.
67. Sun L, Su Y, Jiao A, Wang X, Zhang B. T cells in health and disease. Signal Transduct Target Ther. 2023;8(1):235. https://doi.org/10.1038/s41392-023-01471-y.
68. Prickett TC, McKenzie JL, Hart DN. Adhesion molecules on human tonsil dendritic cells. Transplantation. 1992;53(2):483–90. https://doi.org/10.1097/00007890-199202010-00041.
69. Dustin ML, Springer TA. Role of lymphocyte adhesion receptors in transient interactions and cell locomotion. Annu Rev Immunol. 1991;9:27–66. https://doi.org/10.1146/annurev.iy.09.040191.000331.
70. García-Vallejo JJ, van Liempt E, da Costa MP, et al. DC-SIGN mediates adhesion and rolling of dendritic cells on primary human umbilical vein endothelial cells through LewisY antigen expressed on ICAM-2. Mol Immunol. 2008;45(8):2359–69. https://doi.org/10.1016/j.molimm.2007.11.001.
71. Marth JD, Grewal PK. Mammalian glycosylation in immunity. Nat Rev Immunol. 2008;8(11):874–87. https://doi.org/10.1038/nri2417.
72. He P, Srikrishna G, Freeze HH. *N*-glycosylation deficiency reduces ICAM-1 induction and impairs inflammatory response. Glycobiology. 2014;24(4):392–8. https://doi.org/10.1093/glycob/cwu006.
73. Zhong Y, Li J, Chen Y, Wang JJ, Ratan R, Zhang SX. Activation of endoplasmic reticulum stress by hyperglycemia is essential for Müller cell-derived inflammatory cytokine production in diabetes. Diabetes. 2012;61(2):492–504. https://doi.org/10.2337/db11-0315.
74. Agrawal A, Pulendran B. Anthrax lethal toxin: a weapon of multisystem destruction. Cell Mol Life Sci. 2004;61(22):2859–65. https://doi.org/10.1007/s00018-004-4251-4.
75. Zhu J. T helper 2 (Th2) cell differentiation, type 2 innate lymphoid cell (ILC2) development and regulation of interleukin-4 (IL-4) and IL-13 production. Cytokine. 2015;75(1):14–24. https://doi.org/10.1016/j.cyto.2015.05.010.
76. Gurram RK, Wei D, Yu Q, et al. Crosstalk between ILC2s and Th2 cells varies among mouse models. Cell Rep. 2023;42(2): 112073. https://doi.org/10.1016/j.celrep.2023.112073.
77. Siddiqui ZA, Walker A, Pirwani MM, Tahiri M, Syed I. Allergic rhinitis: diagnosis and management. Br J Hosp Med (Lond). 2022;83(2):1–9. https://doi.org/10.12968/hmed.2021.0570.
78. Fang SB, Zhang HY, Wang C, et al. Small extracellular vesicles derived from human mesenchymal stromal cells prevent group 2 innate lymphoid cell-dominant allergic airway inflammation through delivery of miR-146a-5p. J Extracell Vesicles. 2020;9(1):1723260. https://doi.org/10.1080/20013078.2020.1723260.
79. Sun L, Sha J, Meng C, Zhu D. Mesenchymal stem cell-based therapy for allergic rhinitis. Stem Cells Int. 2020;2020:2367524. https://doi.org/10.1155/2020/2367524.
80. Yan L, Zheng H, Zhang H, Dai L, Zhang Q. Is mesenchymal stem cell effective for allergic rhinitis? A protocol for a systematic review and meta-analysis. BMJ Open. 2022;12(10): e062435. https://doi.org/10.1136/bmjopen-2022-062435.
81. Hood JL. The association of exosomes with lymph nodes. Semin Cell Dev Biol. 2017;67:29–38. https://doi.org/10.1016/j.semcdb.2016.12.002.
82. Ding Y, Wang L, Li H, et al. Application of lipid nanovesicle drug delivery system in cancer immunotherapy. J Nanobiotechnol. 2022;20(1):214. https://doi.org/10.1186/s12951-022-01429-2.
83. Liang Y, Iqbal Z, Lu J, et al. Cell-derived nanovesicle-mediated drug delivery to the brain: principles and strategies for vesicle engineering. Mol Ther. 2023;31(5):1207–24. https://doi.org/10.1016/j.ymthe.2022.10.008.
84. Hussain A, Rafeeq H, Munir N, et al. Dendritic cell-targeted therapies to treat neurological disorders. Mol Neurobiol. 2022;59(1):603–19. https://doi.org/10.1007/s12035-021-02622-4.
85. Vanti G, Wang M, Bergonzi MC, Zhidong L, Bilia AR. Hydroxypropyl methylcellulose hydrogel of berberine chloride-loaded escinosomes: dermal absorption and biocompatibility. Int J Biol Macromol. 2020;164:232–41. https://doi.org/10.1016/j.ijbiomac.2020.07.129.
86. Risaliti L, Yu X, Vanti G, Bergonzi MC, Wang M, Bilia AR. Hydroxyethyl cellulose hydrogel for skin delivery of khellin loaded in ascosomes: characterization, in vitro/in vivo performance and acute toxicity. Int J Biol Macromol. 2021;179:217–29. https://doi.org/10.1016/j.ijbiomac.2021.02.206.
87. Maschalidi S, Mehrotra P, Keçeli BN, et al. Targeting SLC7A11 improves efferocytosis by dendritic cells and wound healing in diabetes [published correction appears in Nature. 2022 Aug;608(7923):E29. 10.1038/s41586-022-05101-5]. Nature. 2022;606(7915):776–84. https://doi.org/10.1038/s41586-022-04754-6.
88. Tokuyama M, Mabuchi T. New treatment addressing the pathogenesis of psoriasis. Int J Mol Sci. 2020;21(20):7488. https://doi.org/10.3390/ijms21207488.
89. Gardner A, de Mingo PÁ, Ruffell B. Dendritic cells and their role in immunotherapy. Front Immunol. 2020;11:924. https://doi.org/10.3389/fimmu.2020.00924.
90. Yue J, Hao D, Liu S, et al. Research progress of traditional Chinese medicine in the treatment of allergic rhinitis. Heliyon. 2024;10(7): e29262. https://doi.org/10.1016/j.heliyon.2024.e29262.
91. Lim S, Jeong I, Cho J, et al. The natural products targeting on allergic rhinitis: from traditional medicine to modern drug discovery. Antioxidants (Basel). 2021;10(10):1524. https://doi.org/10.3390/antiox10101524.
92. Cheng S, Li Z, Gao R, et al. A pan-cancer single-cell transcriptional atlas of tumor infiltrating myeloid cells. Cell. 2021;184(3):792-809.e23. https://doi.org/10.1016/j.cell.2021.01.010.
93. Kim N, Kim HK, Lee K, et al. Single-cell RNA sequencing demonstrates the molecular and cellular reprogramming of metastatic lung adenocarcinoma. Nat Commun. 2020;11(1):2285. https://doi.org/10.1038/s41467-020-16164-1.
94. Zhou Y, Yang D, Yang Q, et al. Single-cell RNA landscape of intratumoral heterogeneity and immunosuppressive microenvironment in advanced osteosarcoma [published correction appears in Nat Commun. 2021 Apr 30;12(1):2567. 10.1038/s41467-021-23119-7]. Nat Commun. 2020;11(1):6322. https://doi.org/10.1038/s41467-020-20059-6.
95. Scharberg EA, Olsen C, Bugert P. An update on the H blood group system. Immunohematology. 2019;35(2):67–8.
96. Zhao R, Qin W, Qin R, et al. Lectin array and glycogene expression analyses of ovarian cancer cell line A2780 and its cisplatin-resistant derivate

cell line A2780-cp. Clin Proteomics. 2017;14:20. https://doi.org/10.1186/s12014-017-9155-z.
97. Meraz IM, Majidi M, Shao R, et al. TUSC2 immunogene enhances efficacy of chemo-immuno combination on KRAS/LKB1 mutant NSCLC in humanized mouse model. Commun Biol. 2022;5(1):167. https://doi.org/10.1038/s42003-022-03103-7.
98. Parra FL, Frank FM, Alliani BF, Romero EL, Petray PB. Imiquimod-loaded nanoarchaeosomes as a promising immunotherapy against Trypanosoma cruzi infection. Colloids Surf B Biointerfaces. 2020;189: 110850. https://doi.org/10.1016/j.colsurfb.2020.110850.

Publisher's Note